Supplementary Information for

Noncollinear ferrielectricity in a van der Waals crystal

Author Information

Jierui Fu [1,13,†], Gang Wang [2,†], Yingpeng Qi [3,6,†] , Wen He [1,†], Yuqiang Fang [5,6,*], Gang Tang [8], Yanting Peng [8], Dong Wang [9], Zhenjie Guan [1], Xuzhou Sun [5], Shuming Zhang [10], Zunyi Deng [8], Yue Liu [1,13], Jiapeng Wang [1,13], Songge Li [2], Tingting Li [2], Jinjing Zhou [1,13], Yuchen Shang [11], Yankun Yin [11], Zhaoju Yang [10], Jinzhong Wang [1], Yang Ding [9], Dao Xiang [6,7], Liang Zhen [1,13], Jiawang Hong [8,*], Fuqiang Huang [5,6*], Junhao Lin [2,12,14,*], Chengyan Xu [4,*], Yang Li [1,13,*]

Affiliations

1 School of Materials Science and Engineering, Harbin Institute of Technology, Harbin 150001, China

2 State key laboratory of quantum functional materials, Department of Physics, and Guangdong Basic Research Center of Excellence for Quantum Science, Southern University of Science and Technology (SUSTech), Shenzhen 518055, China

3 Suzhou Institute for Advanced Research, University of Science and Technology of China, Suzhou 215123, China

4 Sauvage Laboratory for Smart Materials, School of Materials Science and Engineering, Harbin Institute of Technology (Shenzhen), Shenzhen 518055, China

5 Key Laboratory of Intelligent Creation for Extreme Energy Materials (Ministry of Education), School of Materials Science and Engineering, Shanghai Jiao Tong University, Shanghai 200240, China

6 Zhangjiang Institute for Advanced Study (ZIAS), Shanghai Jiao Tong University, Shanghai 201210, China

7 Key Laboratory for Laser Plasmas (Ministry of Education), School of Physics and Astronomy, Shanghai Jiao Tong University, Shanghai 200240, China

8 School of Aerospace Engineering, Beijing Institute of Technology, Beijing 100081, China

9 Center for High Pressure Science and Technology Advanced Research, Beijing 100193, China

10 School of Physics, Zhejiang University, Hangzhou 310058, China

11 State Key Laboratory of High Pressure and Superhard Materials, College of Physics, Jilin University, Changchun 130012, China

12 Quantum Science Center of Guangdong-Hong Kong-Macao Greater Bay Area (Guangdong), Shenzhen 518045, China

13 MOE Key Laboratory of Micro-Systems and Micro-Structures Manufacturing, Harbin Institute of Technology, Harbin 150080, China

14 Guangdong Provincial Key Laboratory of Advanced Thermoelectric Materials and Device Physics and Shenzhen Key Laboratory of Advanced Quantum Functional

Materials and Devices, Southern University of Science and Technology (SUSTech), Shenzhen 518055, China

†These authors contributed equally to this work

*Corresponding authors Email: fangyuqiang@sjtu.edu.cn (Y. Q. Fang); huangfq@sjtu.edu.cn (F.H.); hongjw@bit.edu.cn (J. W. Hong); linjh@sustech.edu.cn (J. H. Lin); cy_xu@hit.edu.cn (C. Y. Xu); liyang2018@hit.edu.cn (Y. Li)

Table of Contents

Supplementary I. Structure characterization of WO_2Br_2

1. Crystal structure and stoichiometry of WO_2Br_2

Supplementary Table 1 The crystallographic data generated from the single-crystal XRD of WO_2Br_2

Crystal Data	
CCDC	2465005
Chemical formula	Br_2O_2W
Mr	375.67
Crystal system, space group	Monoclinic, *Cc*
Temperature (K)	273
a, b, c (Å)	15.468 (2), 3.8645 (5), 7.6801(9)
α, β, γ (°)	90, 104.346 (5),90
V(Å^3)	447.78 (10)
Z	4
Radiation type	Mo *Kα*
μ(mm^{-1})	43.77
No. of measured, independent and observed [$I > 2\sigma(I)$] reflections	3474, 778, 776
R_{int}	0.044
$(\sin\theta/\lambda)_{max}$ (Å^{-1})	0.595
$R[F^2 > 2\sigma(F^2)]$, $wR(F^2)$, S	0.049, 0.118, 1.21
No. of reflections	778
No. of parameters	47
No. of restraints	14
$\Delta\rho_{max}$, $\Delta\rho_{min}$ (e/Å^3)	4.87, −4.85

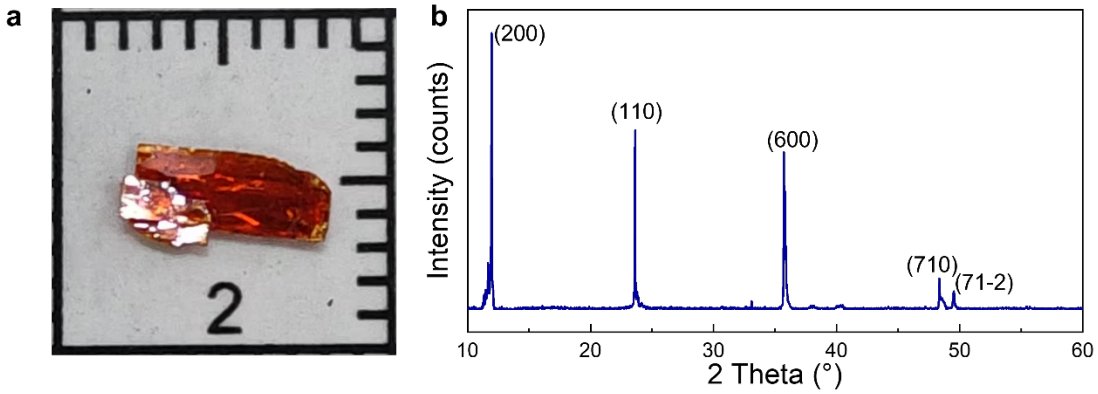

Supplementary Fig. 1 Optical images and X-ray diffraction (XRD) results of the as-prepared WO_2Br_2 single crystals. (a) Macroscopic optical image of WO_2Br_2 single crystals (The side length of the black square is 1 cm, and every small grid corresponds to 1 mm) (b) Indexed-XRD of WO_2Br_2 crystal.

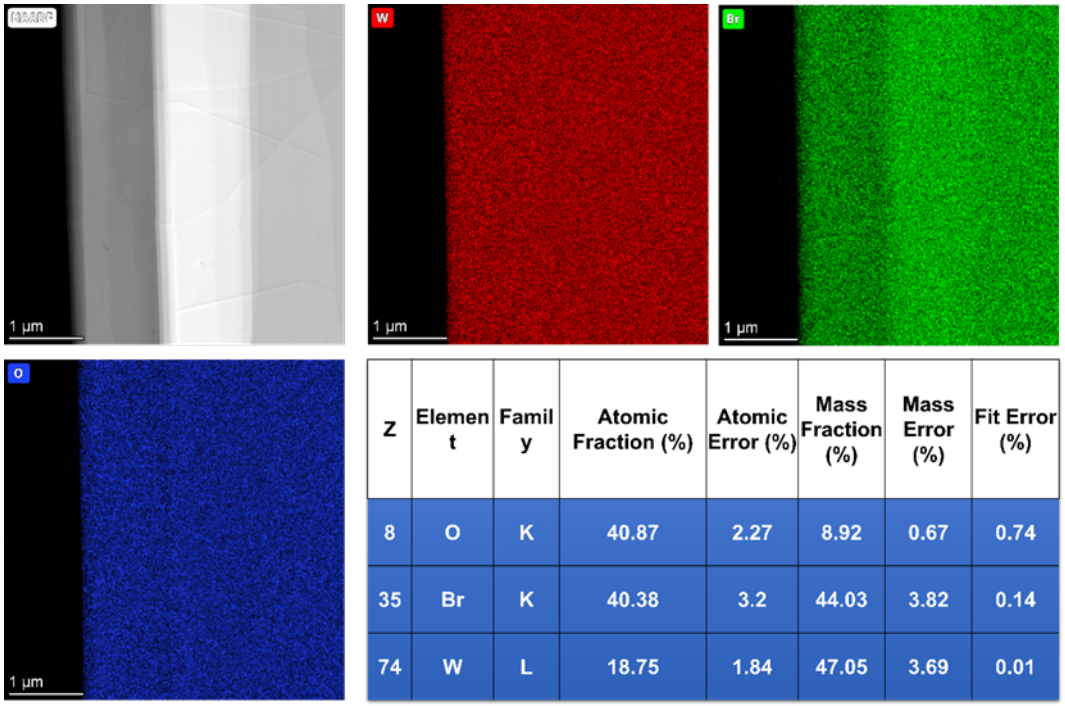

Z	Element	Family	Atomic Fraction (%)	Atomic Error (%)	Mass Fraction (%)	Mass Error (%)	Fit Error (%)
8	O	K	40.87	2.27	8.92	0.67	0.74
35	Br	K	40.38	3.2	44.03	3.82	0.14
74	W	L	18.75	1.84	47.05	3.69	0.01

Supplementary Fig. 2 Low-magnification STEM characterization and EDS elemental mapping of W, Br, and O and quantitative atomic fraction of WO_2Br_2.

2. Electron diffraction and atomic-resolution HAADF-STEM imaging of WO_2Br_2

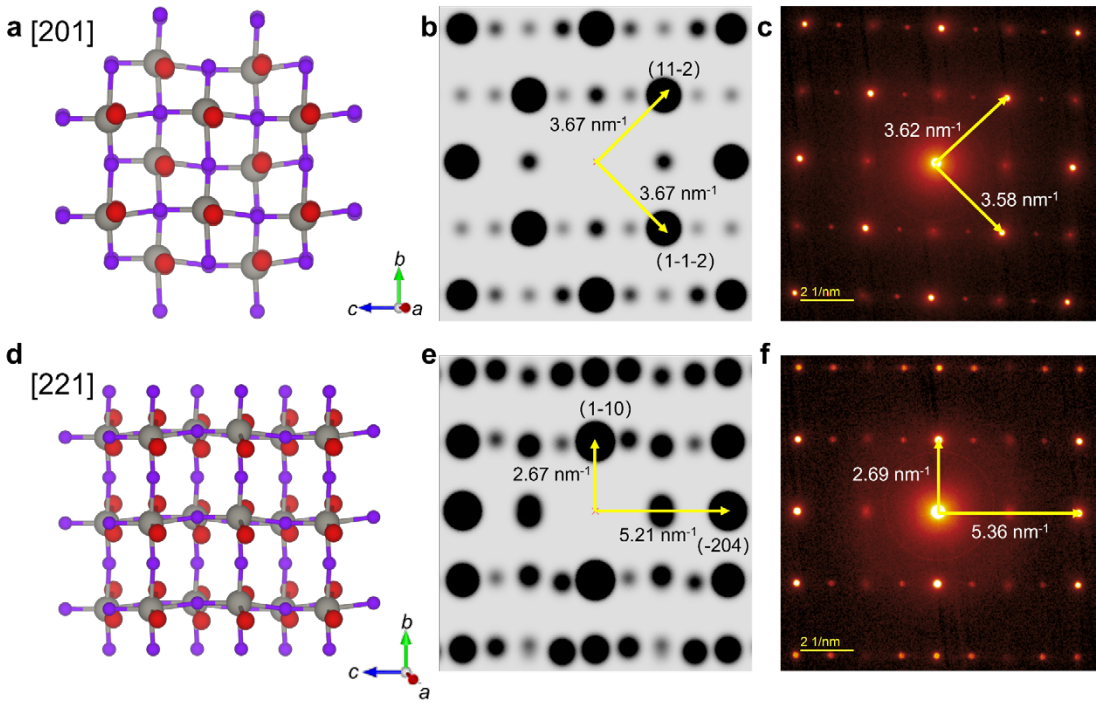

Supplementary Fig. 3 Simulated and experimental electron diffraction patterns corresponding to [201] and [221] zone axes. (a) Atomic arrangement along [201] zone axis. (b) Corresponding simulated and (c) experimental electron diffraction patterns. (d), (e) and (f) for [221] zone axis.

We first conducted an in-plane atomic structure analysis along the [201] direction. **Supplementary Fig. 4a** displays atomic-resolution HAADF-STEM imaging along the [201] zone axis, with the corresponding structural model shown in the inset. Enlarged views (**Supplementary Fig. 4b**) reveal a precise alignment of W atoms along the horizontal directions. Integrated differential phase contrast (iDPC) imaging (**Supplementary Fig. 4c**) identifies oxygen columns between W sites, with white rhombuses highlighting the minimal octahedral cages. While there is a geometric coincidence between the centroids of the W columns and the centers of the octahedra, this does not suggest paraelectric behavior. This is primarily due to the AB stacking configuration and the overlap of Br columns in projection, which ultimately averages out the polarization features within individual layers.

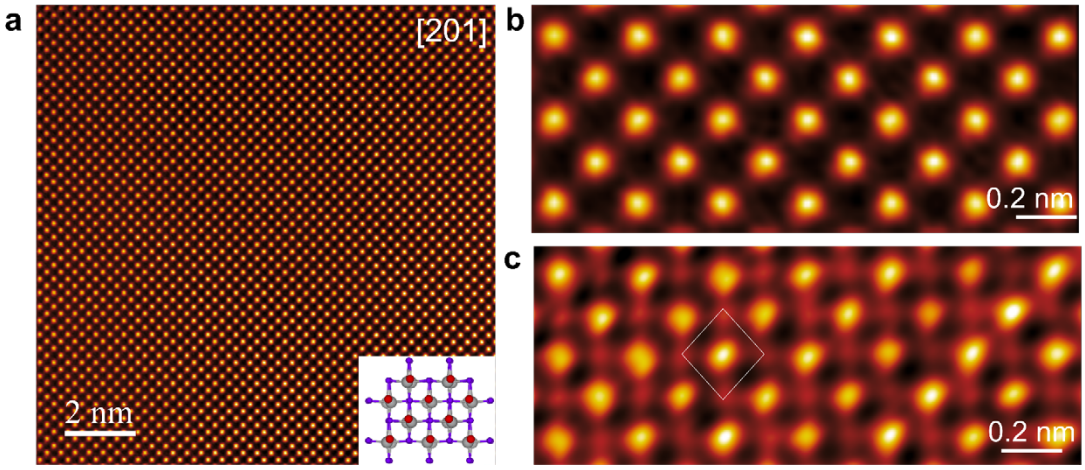

Supplementary Fig. 4 HAADF-STEM images of few-layer WO_2Br_2 along [201] zone axes, with insets displaying corresponding atomic model. (a) Low-magnification HAADF-STEM image; (b) Enlarged HAADF-STEM and (c) iDPC images of the [201] zone axis. The AB stacking obscures antiferroelectric W column shifts due to overlapping atomic projections.

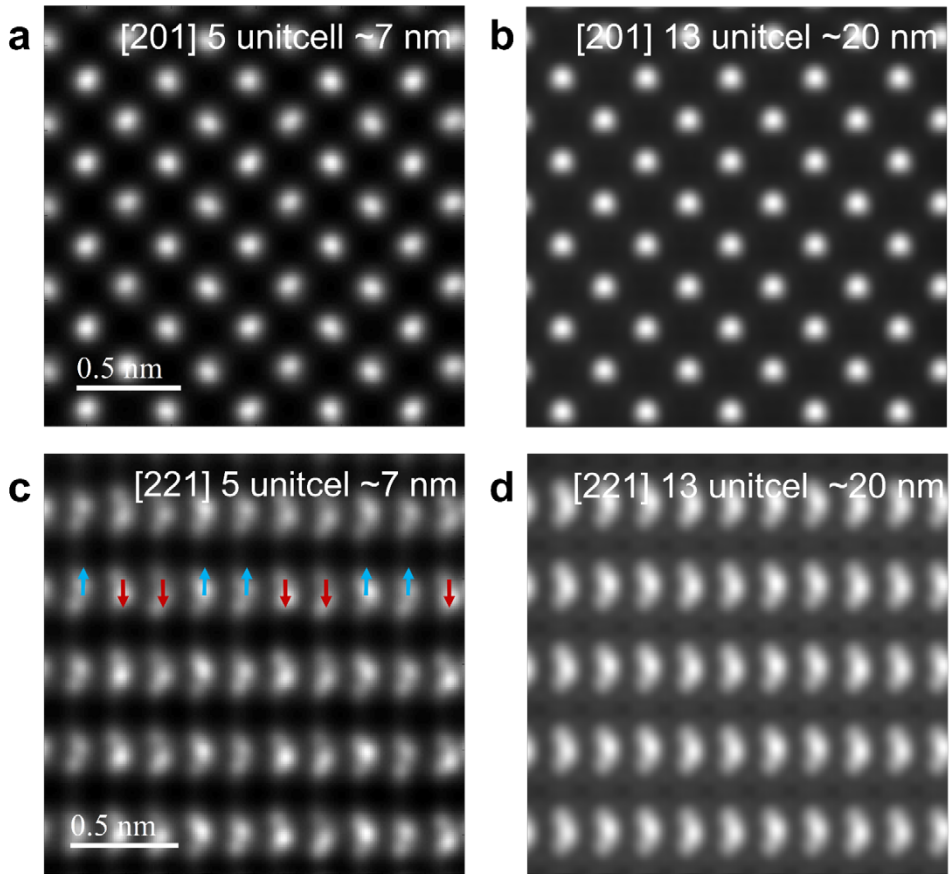

Supplementary Fig. 5 Multi-slice simulated HAADF-STEM image series for thickness-dependent structural analysis of WO_2Br_2. (a, b) Simulated images along the [201] zone axis at sample thicknesses of 7 nm and 20 nm, respectively. (c, d) Corresponding simulations along the [221] zone axis under identical thickness conditions. The simulations highlight the thickness-dependent visibility of W atomic column displacement.

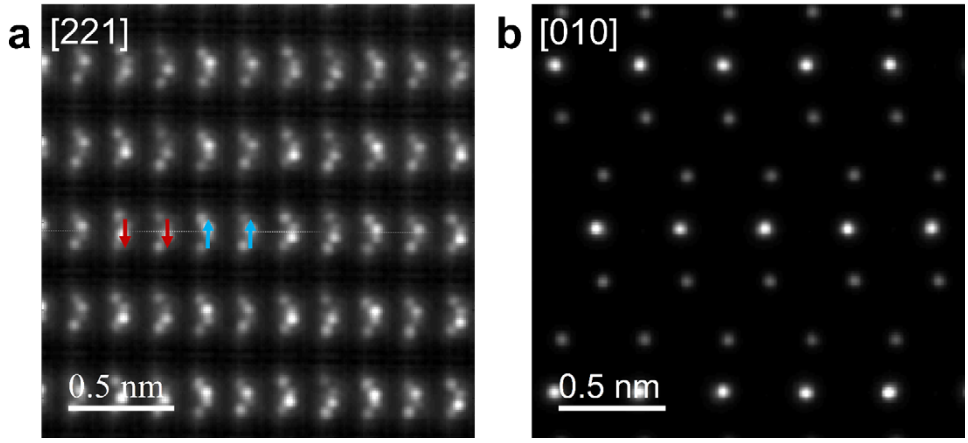

Supplementary Fig. 6 Multislice simulations of WO_2Br_2. (a) Simulated aberration-free HAADF-STEM image of WO_2Br_2 viewed along the [221] zone axis. (b) Corresponding simulation along the [010] zone axis. These ideal-probe multislice calculations, based on the relaxed cif structure, yield antipolar displacements of ± 0.22 Å for the [221] direction and polar displacements of 0.27 Å for the [010] direction.

Because the unsaturated bonds at exposed surfaces are highly reactive, cross-sectional WO_2Br_2 specimens are particularly vulnerable. **Supplementary Fig. 7** shows the evolution of structural degradation as the air-exposure time increases from 1 to 30 minutes. As seen in **Supplementary Fig. 7**a and b, cross-sectional specimens prepared and transferred entirely under inert-gas protection exhibit large-area, uniform ferroelectric displacements along [010]. In contrast, specimens exposed to air for approximately 1 minute (**Supplementary Fig. 7**c, d) already display clear signatures of depolarization, including reversed ionic displacements in certain regions and preservation of the intrinsic polarization only within small local domains. With further exposure (~10 min and 30 min; **Supplementary Fig. 7**e, f), the WO_2Br_2 lattice undergoes pronounced deterioration and eventually becomes amorphous. These results collectively demonstrate that a fully air-free preparation route is required to faithfully capture the intrinsic polar structure of WO_2Br_2.

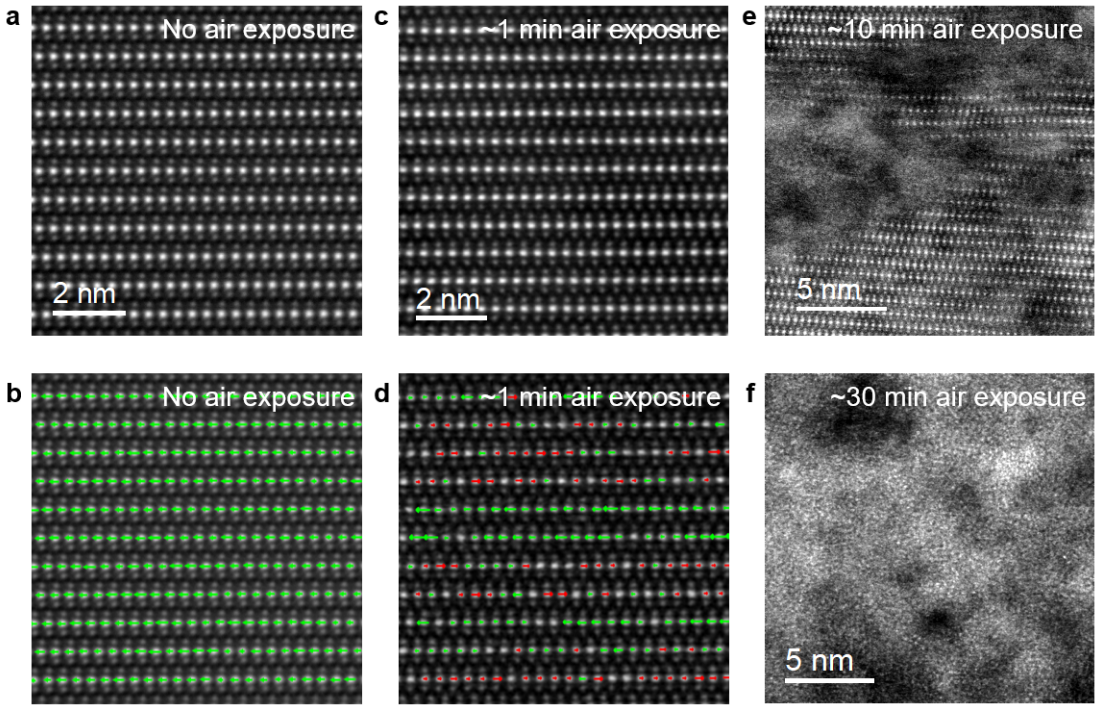

Supplementary Fig. 7 (a) HAADF-STEM image of an inert-protected WO_2Br_2 cross-sectional sample viewed along [010], acquired using a glovebox-integrated focused ion beam (FIB) workflow and inert-transfer double-tilt holder, and (b) the corresponding polarization-vector map showing large-area uniform polar displacements. (c, d) HAADF-STEM image and polarization-vector map of a sample exposed to ambient air for ~1 minute, showing significant structural depolarization and reversed local displacements. (e, f) HAADF-STEM images of samples exposed to air for ~10 and ~30 minutes, respectively, displaying progressive hydrolysis-induced structural degradation and eventual amorphization.

Supplementary Fig. 8 illustrates the experimental setups used for plan-view and cross-sectional measurements, including a glovebox-integrated dry-transfer platform and a focused ion beam (FIB) preparation system, followed by inert-transfer double-tilt TEM loading. This workflow ensures that the specimens are not exposed to air during either milling or transfer.

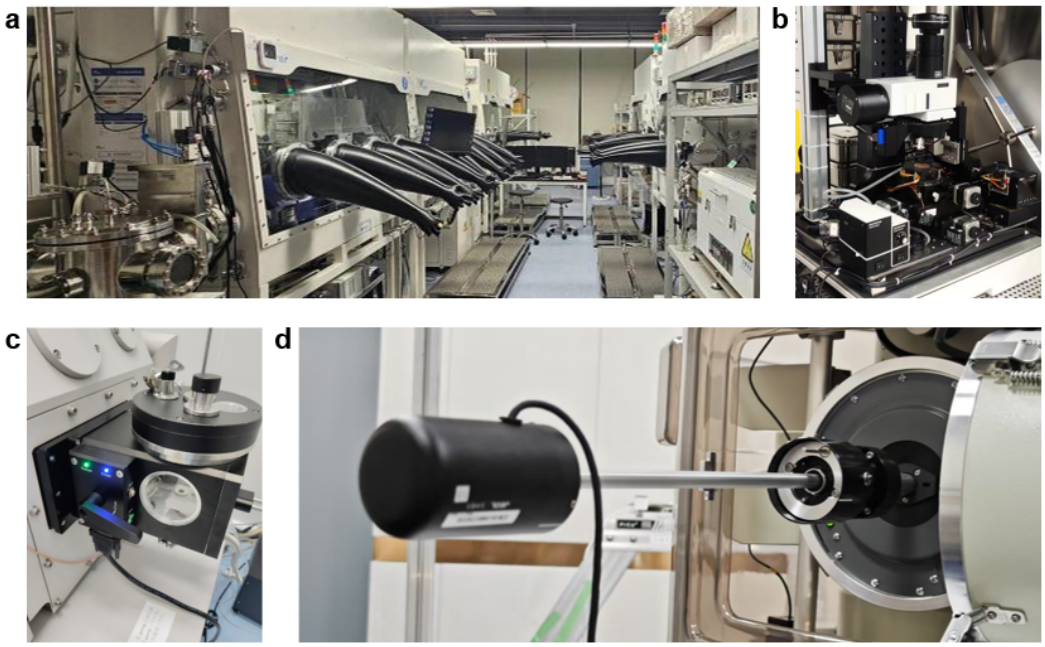

Supplementary Fig. 8 Glovebox-integrated inert preparation and transfer system for WO_2Br_2 TEM specimens. (a) Glovebox-integrated system used for air-free preparation and handling of TEM specimens. (b) Dry-transfer platform for fabricating plan-view samples inside the glovebox. (c) Inert/vacuum transfer module connecting the glovebox to the FIB microscope, enabling oxygen- and moisture-free cross-sectional sample preparation. (d) JEOL inert-transfer double-tilt TEM holder used for air-free loading and imaging.

To verify that the noncollinear dipole structure in WO_2Br_2 is a uniform, long-range feature rather than being confined to small localized regions, we performed large-field-of-view atomic-resolution HAADF-STEM characterization along two crystallographic orientations. Along the [221] zone axis (**Supplementary Fig. 9**), a wide-area (~16 × 16 nm^2) HAADF-STEM image reveals uniform antipolar displacements of W atomic columns across the entire field of view, indicating a spatially homogeneous antipolar arrangement. Along the cross-sectional [010] direction (**Supplementary Fig. 10**), a larger-area (~25 × 25 nm^2) HAADF-STEM image combined with polarization-vector maps derived from full atomic-position fitting shows consistently aligned polar displacements over the entire region. Together, these large-area measurements demonstrate that the noncollinear dipole configuration in WO_2Br_2 persists uniformly across extended continuous regions of the crystal, confirming its intrinsic and long-range nature.

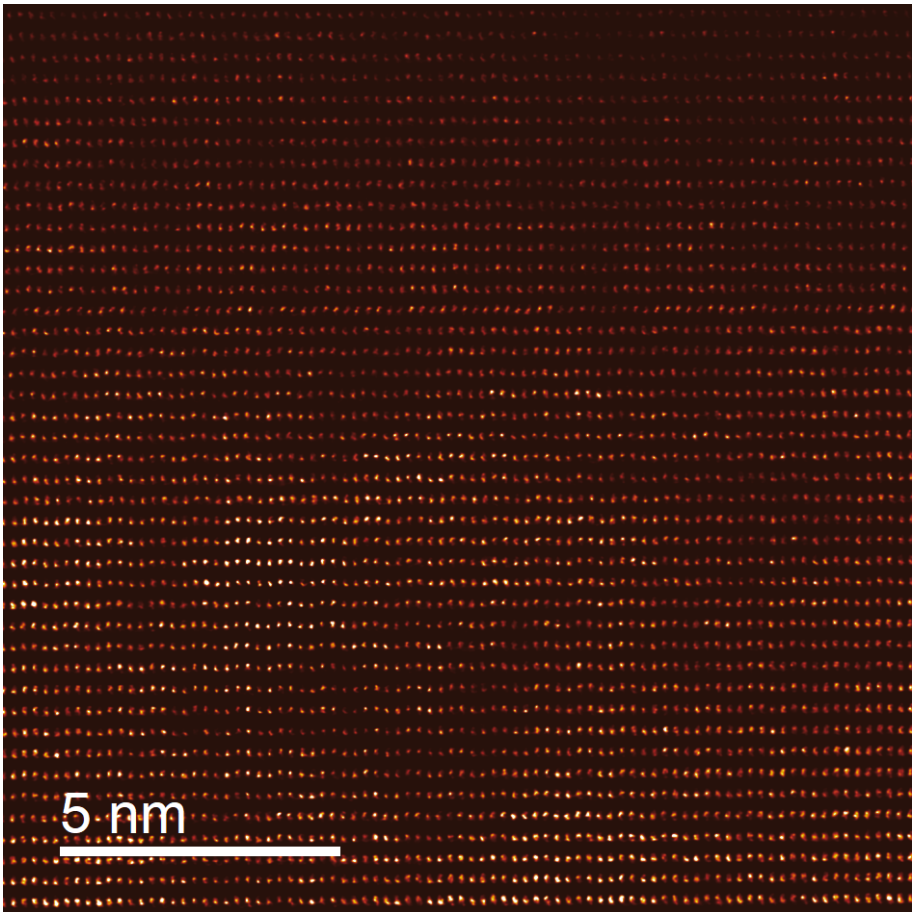

Supplementary Fig. 9 Large-area HAADF-STEM image of WO_2Br_2 viewed along the [221] zone axis, showing uniform antipolar displacements across a ~16 × 16 nm^2 field of view.

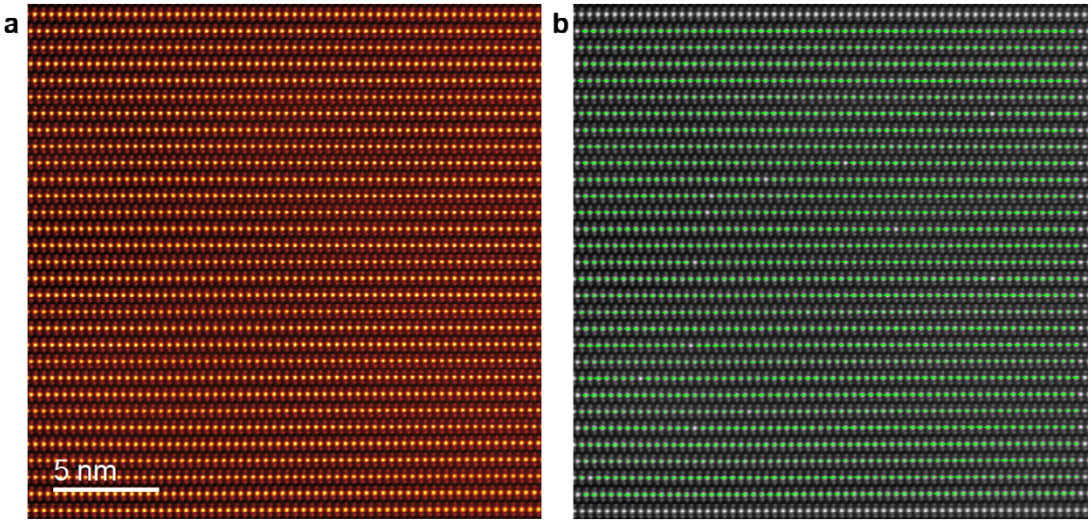

Supplementary Fig. 10 (a) Large-area HAADF-STEM image of WO_2Br_2 viewed along the [010] zone axis. (b) Corresponding polarization-vector map obtained from full atomic-position fitting, showing uniform c-axis polar displacements across the field of view.

As discussed in previous studies[1], the mesoscopic electric field induces a shift in the DPC signal at each atomic column position, resulting in an electric field asymmetry at both W and Br sites. The electric field in ferroelectric materials can be considered to consist of two components: a uniform, long-range (mesoscopic) polarization field, and an atomically localized electric field that resulted from the distribution of valence electrons, which can be influenced by the combined effects of polar structural distortions and charge redistribution within the unit cell. Such atom-scale localized electric field can be detected by the DPC signal.

To better resolve the atomic-scale electric-field features, the experimental DPC dataset was reprocessed using refined normalization combined with mild Gaussian filtering, as shown in **Supplementary Fig. 11a**. Under this processing, electric-field asymmetry is observed simultaneously at both W and Br atomic columns. Notably, the asymmetry at the W columns is substantially more pronounced than that at the Br columns. This difference arises because, in WO_2Br_2, the W^{6+} columns possess a substantially higher effective nuclear charge and a more pronounced polarization-induced charge redistribution than the Br^- columns, giving rise to a stronger local electric-field gradient and hence a more prominent DPC signal asymmetry, which consistent with previous reports[1,2].

To further support this interpretation, DPC simulations were performed based on the polarized atomic structure refined from X-ray diffraction. Using ion scattering factors under experimental conditions, a 4D STEM dataset was simulated and the corresponding DPC signals were extracted. The simulated results are in good agreement with the experimental data. As shown in **Supplementary Fig. 11a**, the simulated W

atomic columns exhibit clear electric-field asymmetry, whereas the asymmetry at the Br columns is comparatively weaker, consistent with the experimental trend.

To exclude specimen tilt as a possible origin of the observed DPC asymmetry, simulated DPC signals of paraelectric WO_2Br_2 were compared at 0° and 0.6° tilt (**Supplementary Fig. 11b, d**) with those of the ferroelectric structure (**Supplementary Fig. 11c**). In the paraelectric structure at 0° tilt, both W and Br atomic columns exhibit symmetric DPC signals. Although a 0.6° tilt introduces apparent DPC asymmetry at both W and Br sites, the magnitude of the asymmetry is comparable for all atomic species. In contrast, for the ferroelectric structure, the DPC asymmetry is significantly more pronounced at the heavier W columns, consistent with expectations for polarization-induced electric fields[1].

In addition to affecting DPC contrast, specimen tilt also leads to asymmetry in HAADF-STEM intensity profiles. As shown in **Supplementary Fig. 11d**, tilted configurations produce a characteristic tailing in the HAADF intensity profile (indicated by red arrows). By comparison, both the experimental HAADF images acquired simultaneously with DPC (**Supplementary Fig. 11a**) and the simulated ferroelectric structure (**Supplementary Fig. 11c**) display symmetric atomic intensity profiles, further indicating that specimen tilt is not responsible for the observed DPC asymmetry.

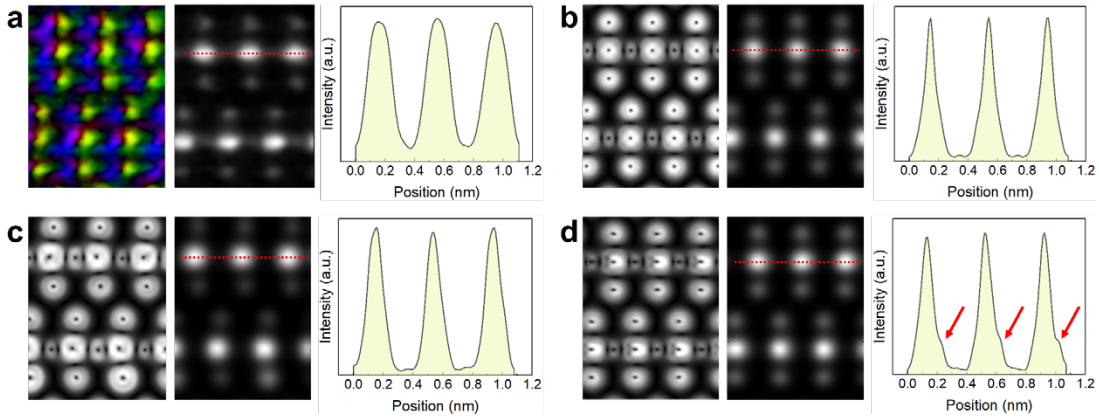

Supplementary Fig. 11 (a) Experimental DPC image of WO_2Br_2 and the simultaneously acquired HAADF image, with the line intensity profile along the red dashed line in the HAADF image. (b-d) Simulated DPC amplitude maps for the paraelectric structure (b), ferroelectric structure (c), and paraelectric structure with 0.6° tilt (d), including the corresponding HAADF images and line intensity profiles along the red dashed lines in the HAADF images. DPC simulations were conducted using ion scattering factors for charged models based on QSTEM, followed by the extraction of simulated DPC signals from the 4D STEM dataset according to experimental conditions using a custom-written Python code.

Although previous studies have shown that defocus-series DPC measurements can help further distinguish genuine polarization-induced fields from tilt-related artifacts[1],

such measurements are not feasible here due to the limited beam stability of the halide samples. Nevertheless, the combined evidence from refined DPC processing, structure-based simulations, tilt comparison, and large-area polarization mapping demonstrates that the observed atomic-scale electric-field asymmetry originates from intrinsic ferroelectric polarization.

Supplementary II. DFT Calculation of noncollinear polarization in WO_2Br_2

Previous work has confirmed that two-dimensional MO_2X_2 (M: group-VI transition metal; X: halogen) has non-collinear intrinsic ferroelectric properties[3]. We wonder whether this property also exists in bulk WO_2Br_2. To evaluate the ferroelectric phase structural transition, the centrosymmetric phase (paraelectric state) of WO_2Br_2 should be determined. Starting from the *Cc* phase (space group No.9), we obtained the centrosymmetric phase (paraelectric state) with space group *C2/m* (space group No.12) according to the pseudocode of the Bilbao crystallographic server[4–6]. The paraelectric (PE) structure of WO_2Br_2 is shown in **Supplementary Fig. 12a**, where the W ion is located at the center of the octahedron. There are two main imaginary frequency branches in its phonon spectrum, which will lead to spontaneous distortions. According to the symmetry analysis, the Γ_2^- vibration mode will lead to FE-type distortion; The A_2^+ vibration mode will lead to AFE-type distortion. The coupling state of the two vibration modes causes the structure to transform from PE phase to FiE phase. The ordering directions of W-Br in FE and AFE structures are along *c*-axis and *b*-axis respectively, and non-collinear dipole moment is generated in FiE structure under coupling condition.

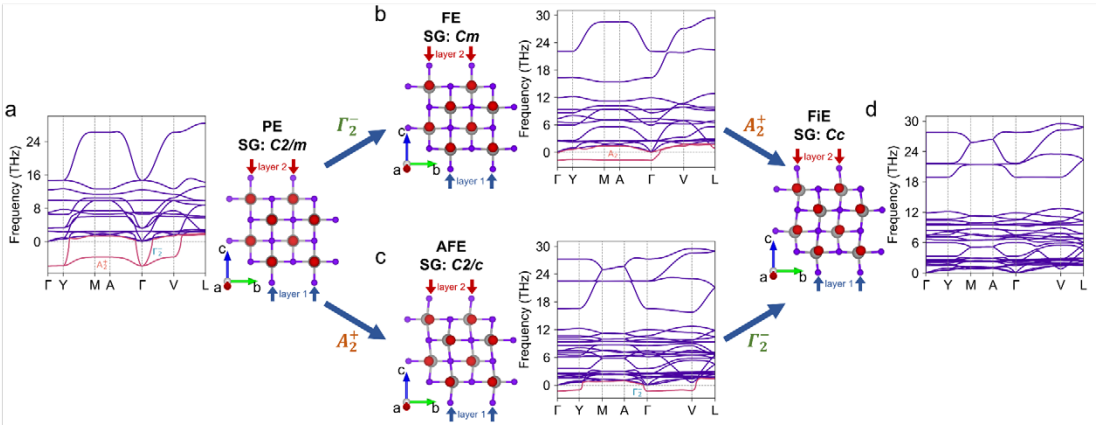

Supplementary Fig. 12 Noncollinear ferrielectricity of WO_2Br_2. The imaginary-frequency branches of phonons are displayed in red. (a) The PE phase. The unstable vibration modes (Γ_2^- and A_2^+) are noted. (b) The FE phase. The intermediate states obtained from a single vibration mode Γ_2^-. (c) The AFE phase. The inntermediate states obtained from a single vibration mode A_2^+. (d) The FiE phase. The stable state obtained by coupling Γ_2^- and A_2^+ vibration modes.

Supplementary Table 2 Mode amplitudes (in Å) associated with the symmetry-mode decompositions along the structural transition pathways.

$C2/m \rightarrow Cm$	$C2/m \rightarrow C2/c$	$C2/c \rightarrow Cc$	$Cm \rightarrow Cc$
$Q_{\Gamma_2^-}$= 0.5867 Å	$Q_{A_2^+}$= 0.1344 Å	$Q_{\Gamma_2^-}$= 0.2775 Å	$Q_{A_2^+}$= 0.1302 Å

In WO_2Br_2 there are two relevant soft modes in the high-symmetry paraelectric reference: a Γ-point FE mode that drives polar displacements along c, and an A-point AFE mode that drives antipolar displacements along b. Phonon calculations show that both modes are unstable in the paraelectric phase. Freezing only one of them (FE or AFE) still leaves the other branch unstable, so the structure cannot be fully stabilized by a single-order-parameter distortion. By contrast, when both modes condense simultaneously, the resulting noncollinear structure is dynamically stable and has a lower total energy than the hypothetical "FE-only" or "AFE-only" structures.

We have performed a systematic analysis of the potential energy surface (PES), as shown in **Supplementary Fig. 13** Both Γ_2^- and A_2^+ exhibit double-well potentials. When the two modes are introduced simultaneously, the total energy is further reduced relative to the configurations in which only Γ_2^- and or only A_2^+ is activated. This behavior clearly demonstrates the presence of a cooperative biquadratic coupling between the two modes, which stabilizes the resulting noncollinear dipole configuration. Similar cooperative interactions have been reported in related materials systems[7,8].

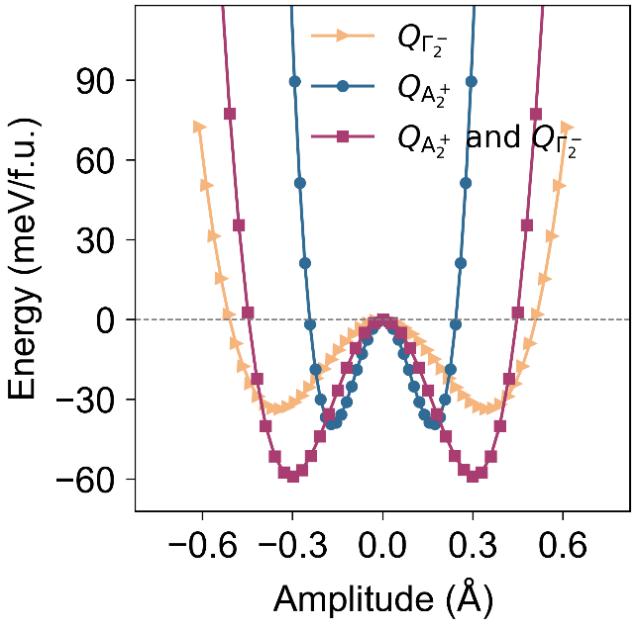

Supplementary Fig. 13 The potential energy surface (PES) as a function of $Q_{\Gamma_2^-}$, $Q_{A_2^+}$, and $Q_{A_2^+} + Q_{\Gamma_2^-}$

Berry-phase polarization calculations reveal that the calculated spontaneous polarizations reach 4.44 μC/cm^2 along the [100] direction and 17.84 μC/cm^2 along the [001] direction, which means the spontaneous polarization of WO_2Br_2 is dominated by the polarization along *c*-axis.

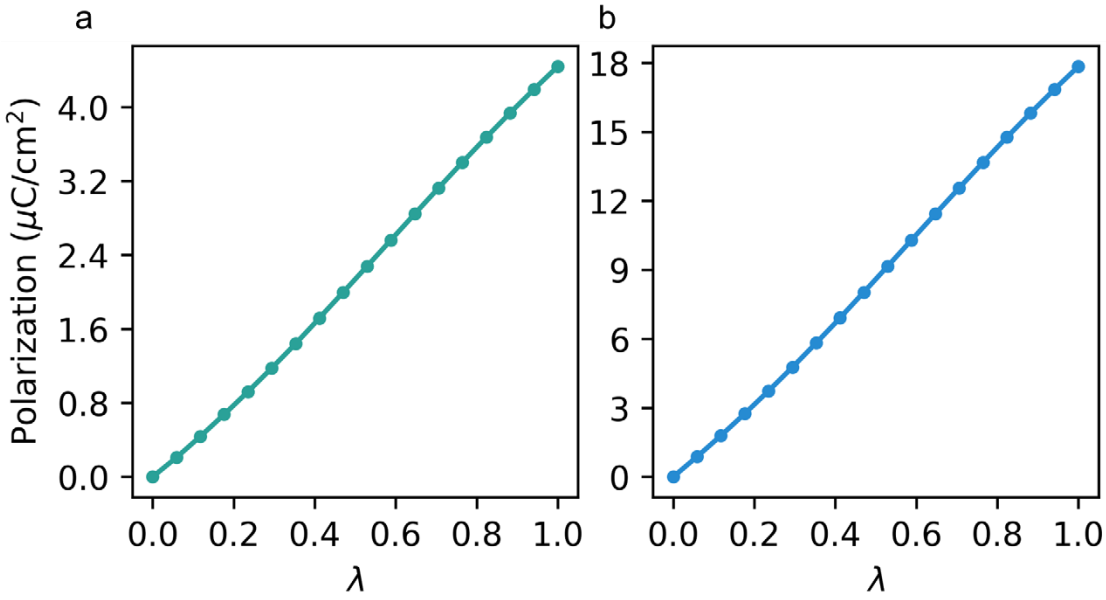

Supplementary Fig. 14 Calculated spontaneous polarization as a function of the normalized displacement (λ) along the (a) [100] (*a*-axis) and (b) [001] (*c*-axis) directions.

Supplementary III. Ferroelectricity of WO_2Br_2

1. PFM signals of the Au-coated Si substrate as a reference

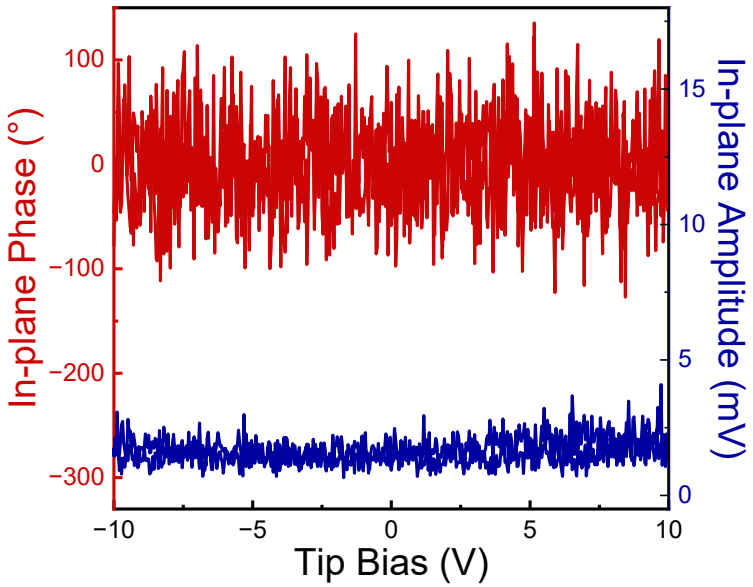

Supplementary Fig. 15 Absence of hysteretic behavior in PFM amplitude and phase measurements on Au-SiO_2/Si Substrate

2. In-plane and out-of-plane PFM signals of WO_2Br_2

Supplementary Fig. 16 shows side-by-side in-plane and out-of-plane PFM images (amplitude and phase). In **Supplementary Fig. 16a**, **c** and **e**, across a representative domain boundary, the in-plane PFM phase shows a clear 180° contrast, and the amplitude is strongly suppressed at the wall, which are characteristic features of ferroelectric domains and domain walls, indicating the opposite in-plane polarization orientations on the two sides, with the polarization direction parallel to the wall. By contrast, the out-of-plane PFM signals show no corresponding contrast in either amplitude or phase in the same region. Taken together, the data show that domains that are antiparallel in-plane do not differ out-of-plane; thus, the in-plane and out-of-plane components are not directly linked in WO_2Br_2. For reference, this differs from α-In_2Se_3 or $BiFeO_3$[9–14], where the two components can be intercorrelated. Accordingly, these results provide experimental support for focusing primarily on in-plane polarization in this work.

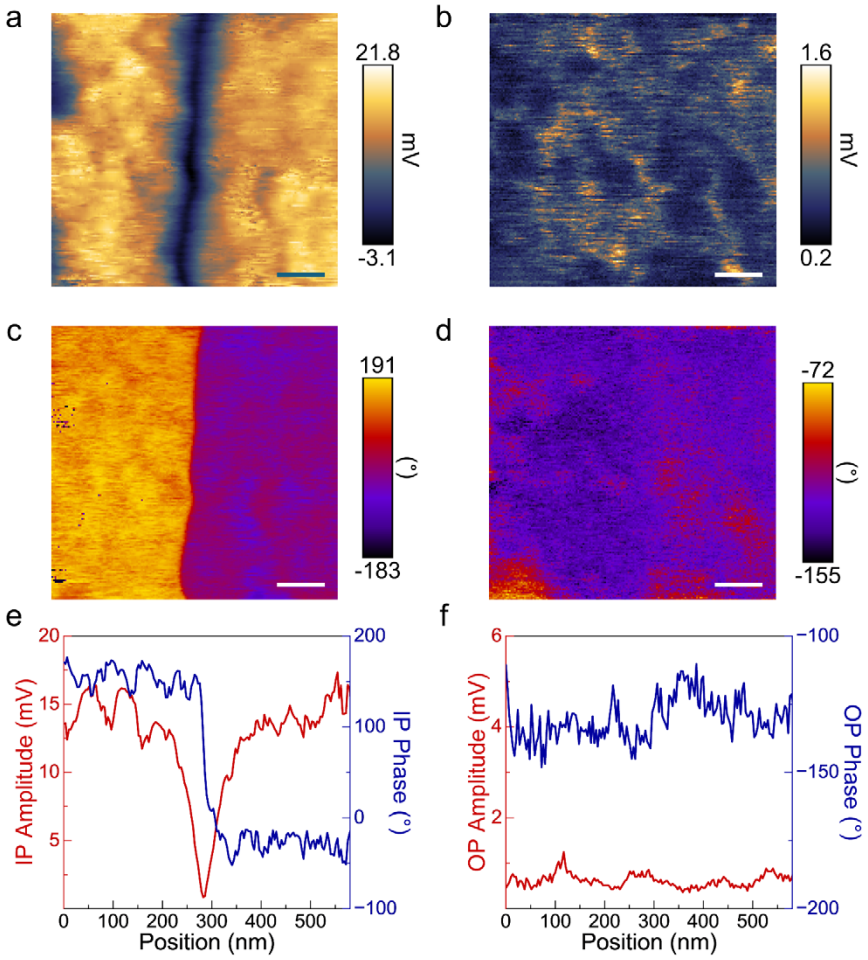

Supplementary Fig. 16 In-plane and out-of-plane PFM signals of WO_2Br_2 near a domain wall. (a, c, e) In-plane PFM amplitude (a) and phase (c) images together with the corresponding line profiles (e). (b, d, f) Out-of-plane PFM amplitude (b) and phase (d) images from the same region and the corresponding line profiles (f). Scale bars in (a–d), 200 nm.

3. Domain-wall configuration of WO_2Br_2

In layered transition-metal oxyhalides such as $NbOCl_2$ and $NbOI_2$, exfoliated flakes are frequently single-domain[15–18], which likely reflects relatively high domain-wall energies in this materials class; recent studies on $NbOI_2$ further show that, in addition to the more common neutral walls, head-to-head and tail-to-tail charged walls can also occur and be stabilized by local structural irregularities or defects[19], suggesting by analogy that both wall types may exist in WO_2Br_2.

Experimentally, exfoliated WO_2Br_2 flakes generally exhibit a low native domain density, and most samples are single-domain, consistent with observations in $NbOI_2$ and $NbOCl_2$, whereas a subset of flakes shows spontaneously formed ferroelectric domains. In such cases, domain walls often nucleate at sample edges, extend into the interior, and terminate within the flake; boundaries between differently oriented domains are typically not straight but display a zig-zag or meandering morphology (**Supplementary Fig. 17**), which is consistent with the behavior widely associated with charged (head-to-head) walls that undulate to reduce electrostatic and wall energies, while in other samples the walls run parallel to the scan direction and appear comparatively rectilinear (**Supplementary Fig. 16**, **Supplementary Fig. 18**), in line with the characteristics of neutral walls. Taken together, WO_2Br_2 commonly appears as single-domain, and in those samples where domains are present we observe both neutral and head-to-head charged walls, with the latter often stabilized or guided by local topographic defect.

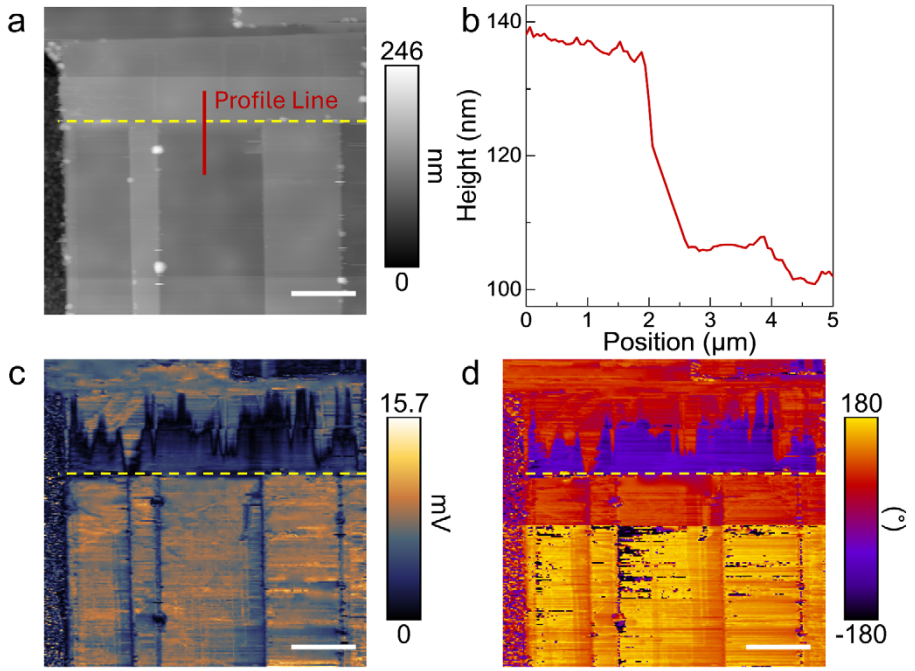

Supplementary Fig. 17 Domains and charged domain walls in a region with pronounced height variation inside a WO_2Br_2 flake. (a) AFM topography. (b) Height profile along the red line in (a), showing a significant height difference. (c) In-plane PFM amplitude. (d) In-plane PFM phase. Scale bar in (a, c, d): 3μm.

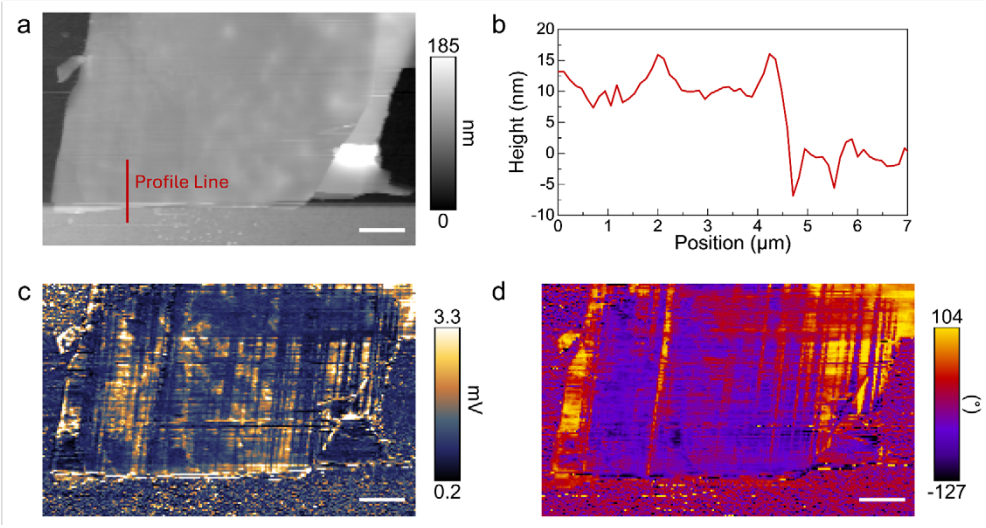

Supplementary Fig. 18 Domains and neutral domain walls in a region with pronounced height variation at the edge of a WO_2Br_2 flake. In contrast to charged domain walls, neutral domain walls are oriented perpendicular to the tip scan direction and exhibit a straighter geometry. (a) AFM topography. (b) Height profile along the red line in (a), showing a significant height difference. (c) In-plane PFM amplitude. (d) In-plane PFM phase. Scale bar in (a, c, d): 3μm.

4. Reversible ferroelectric switching in WO_2Br_2

The reversal of ferroelectric polarization is achieved by applying different voltages to a single point on the sample. From the sample edge geometry and polarized SHG spectra we determined that the probe scanning direction is approximately perpendicular to the spontaneous polarization direction. We then positioned the probe at the midpoint marked in **Supplementary Fig. 20** and applied a DC bias of –12 V via the tip. After bias application, the surface topography shows no discernible change, whereas the in-plane PFM amplitude and phase exhibit pronounced differences: the region immediately above the biased site displays a phase offset of about 180° relative to its surroundings, while the lower half of the field remains unchanged. Because the voltage was applied at a single point, the effective switching field is spatially limited and does not induce large-area reversal; instead, an isolated, island-like switched domain forms above the midpoint. Furthermore, after the isolated domain forms and about 30 minutes delay, the upper island domain spontaneously expands and connects with the surrounding region of the same polarization orientation. The out-of-plane PFM amplitude and phase at this stage were measured, which exhibit no obvious, concomitant changes (**Supplementary Fig. 19**); accordingly, in the subsequent biasing sequence we present only the in-plane PFM amplitude and phase.

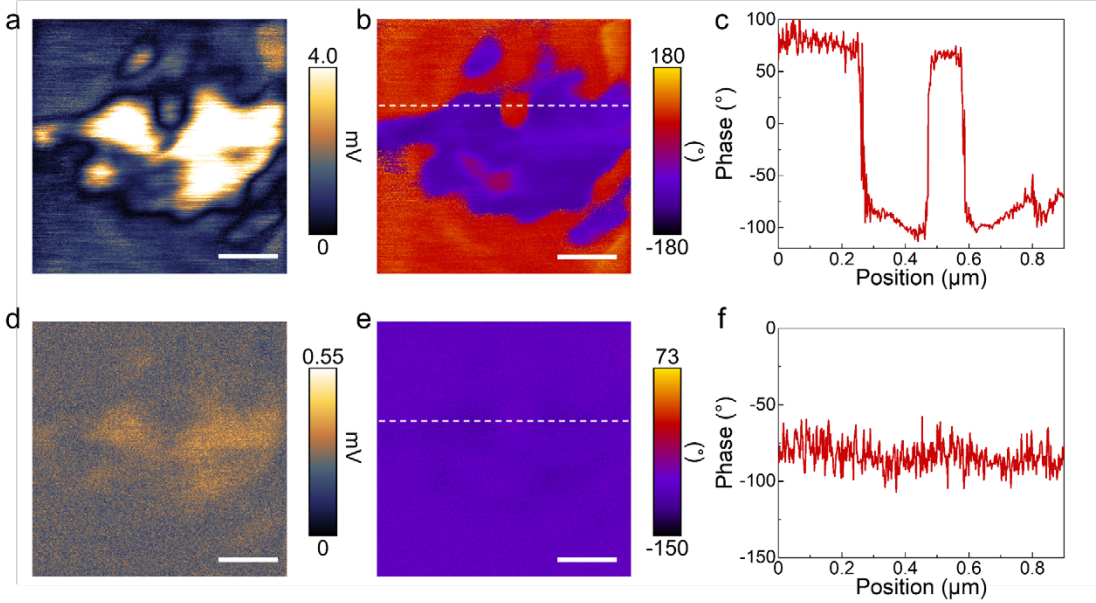

Supplementary Fig. 19 In-plane and out-of-plane PFM signals of WO_2Br_2 after applying a local voltage at a single point. (a, b, c) In-plane PFM amplitude (a), phase (b) and corresponding line profile (c) taken along the white dashed line in (b). (d, e, f) Out-of-plane PFM amplitude (d), phase (e) and corresponding line profile (c) taken along the white dashed line in (e).

After polarized at the midpoint of **Supplementary Fig. 20**, we the applied –12 V at a location below the original domain. Compared to the initial isolated domain experiment, domain formation and expansion in this second instance was much easier

— immediately after bias application, a large-area ferroelectric domain reversal appeared. We attribute this to the fact that the formation of the isolated domain reduced the energy barrier for domain nucleation and wall motion, making reversal easier.

After large-area reversal, we then applied a +10 V bias to test reversibility. After +10 V application, within the original region we again observed a region showing nearly 180° phase reversal relative to the surrounding, essentially replicating the effect seen with the initial –12 V bias. Therefore, these experiments demonstrate that an applied field can write ferroelectric domains in WO_2Br_2 and that the polarization reversal is reversible.

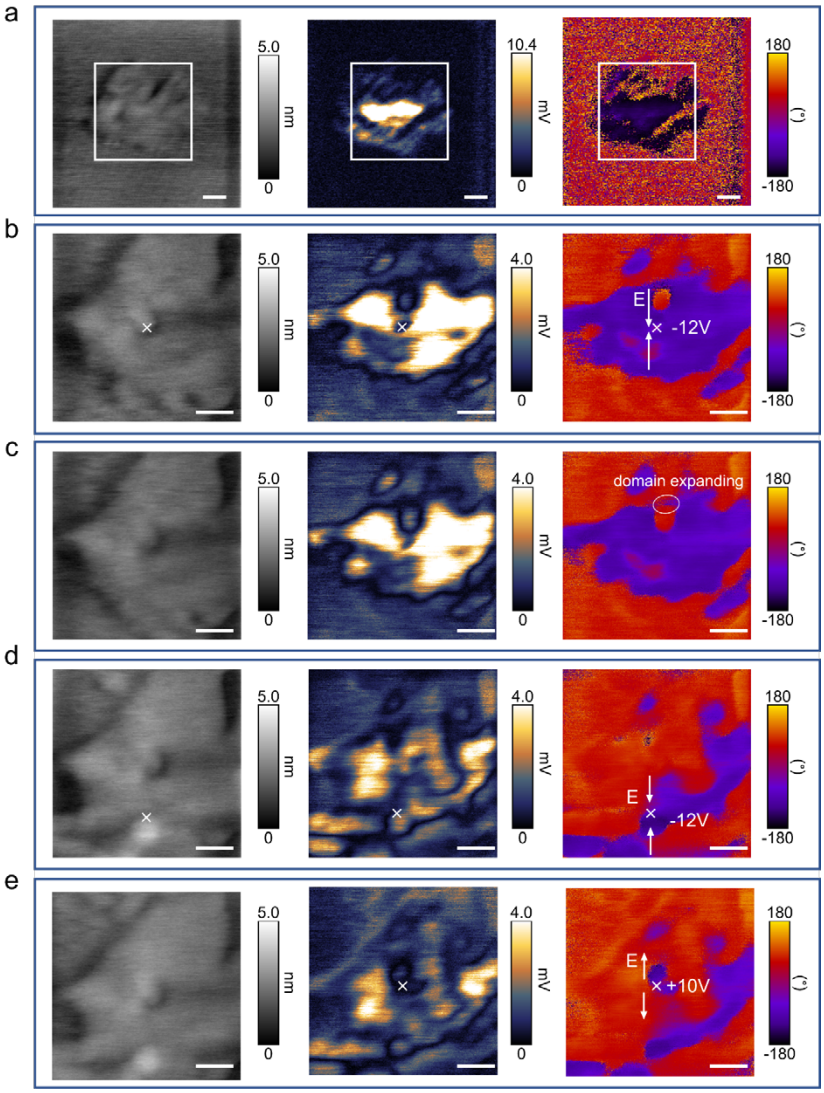

Supplementary Fig. 20 Evolution of domain nucleation and reversal during local voltage application at a single point. Left column: topography; middle column: in-plane PFM amplitude; right column: in-plane PFM phase. (a) Initial topography and PFM signals. (b) Topography and PFM signals after applying −12 V at the marked position. (c) Topography and PFM signals 30 min after the state shown in (b). (d) Topography and PFM signals after applying −12 V at the marked position again. (e) Topography and PFM signals after applying +10 V at the marked position.

5. Uniaxial ferroelectric behavior of WO_2Br_2

Uniaxial ferroelectric behavior was determined by P-E measurements on bulk specimens along two crystallographic axes; the polar axis and the non-polar axis were identified via polarized SHG. The results are shown in **Supplementary Fig. 21**. Although significant leakage current is present, the P-E loop along the polar axis still shows a clear hysteresis; concurrently, the I-E curve exhibits two distinct peaks, which are evidence of domain switching during the field cycle. In contrast, along the non-polar axis the P-E curve shows a purely resistive behavior and the I-E curve is nearly linear and without any drastic change, indicating absence of ferroelectric or antiferroelectric behavior in the non-polar direction. In other words, WO_2Br_2 exhibits uniaxial ferroelectric behavior. Further, PFM maps measured at different probe orientations (**Supplementary Fig. 22**) show that a clear amplitude signal appears only when the probe is aligned with the polarization axis; when the probe is aligned to the non-polar axis, the amplitude response is at the level of the non-piezoelectric substrate, further evidencing uniaxial ferroelectricity.

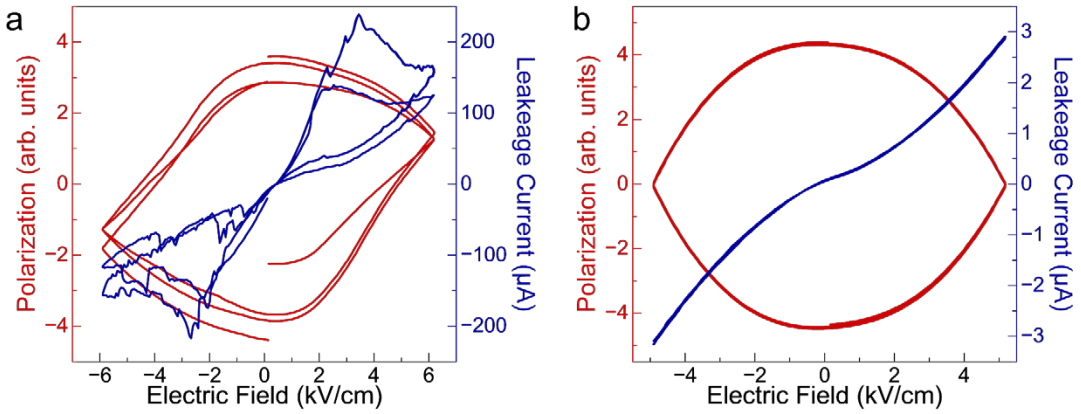

Supplementary Fig. 21 P–E and I–E curves of WO_2Br_2 measured along the polarization and antipolar directions. (a) Polarization direction. (b) Antipolar direction. Although measurements along the polarization direction suffer from relatively large leakage current, a ferroelectric-like hysteresis in polarization and pronounced current peaks are still observed. In contrast, measurements along the antipolar direction exhibit a predominantly capacitive response, with no obvious hysteresis in either polarization or current.

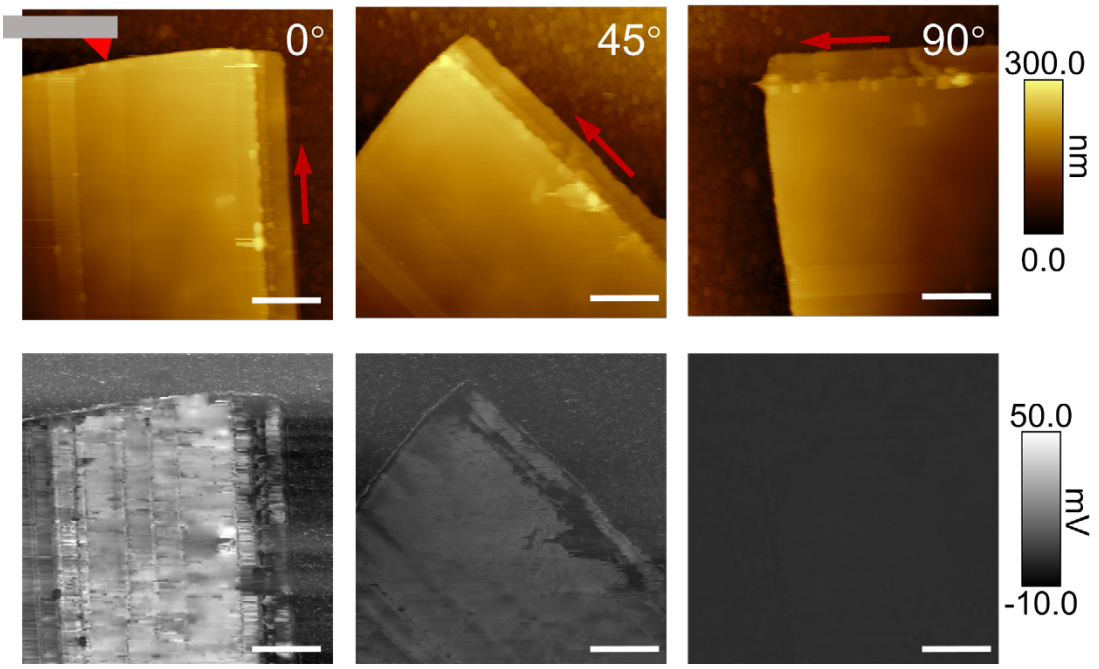

Supplementary Fig. 22 In-plane PFM amplitude of WO_2Br_2 measured at different relative angles between the tip and the sample.

Supplementary IV. SHG of WO_2Br_2

1. Polarization-resolved SHG of WO_2Br_2 based on point-group analysis: first-principles calculations and experimental data

Specifically, our SHG measurements were performed in a back-reflection configuration (**Supplementary Fig. 23**). Under our normal-incidence condition, the incident fundamental field lies in the sample plane, so we model the input as:

$$\mathbf{E}(\omega) = E_0(\cos\theta\,,\ \sin\theta\,,0) \qquad (S1)$$

where θ is the angle of the polarization direction of the incident light with respect to the crystal x-axis. The nonlinear polarization is written as:

$$\mathbf{P_i}(2\omega) = \varepsilon_0 \sum_{j,k} \chi^{(2)}_{ijk}\, E_j(\omega) E_k(\omega) \qquad (S2)$$

or

$$\begin{pmatrix} P_x \\ P_y \\ P_z \end{pmatrix} = \varepsilon_0 \begin{pmatrix} \chi^{(2)}_{xxx} & \chi^{(2)}_{xyy} & \chi^{(2)}_{xzz} & \chi^{(2)}_{xyz} & \chi^{(2)}_{xxz} & \chi^{(2)}_{xxy} \\ \chi^{(2)}_{yxx} & \chi^{(2)}_{yyy} & \chi^{(2)}_{yzz} & \chi^{(2)}_{yyz} & \chi^{(2)}_{yxz} & \chi^{(2)}_{yxy} \\ \chi^{(2)}_{zxx} & \chi^{(2)}_{zyy} & \chi^{(2)}_{yzz} & \chi^{(2)}_{zyz} & \chi^{(2)}_{zxz} & \chi^{(2)}_{zxy} \end{pmatrix} \begin{pmatrix} E^2cos^2(\theta) \\ E^2sin^2(\theta) \\ 0 \\ 0 \\ 0 \\ 2Ecos(\theta)\sin(\theta) \end{pmatrix} \qquad (S3)$$

For the monoclinic *Cc* space group (point group *m*, unique *b*), the equation can be written as:

$$\begin{pmatrix} P_x \\ P_y \\ P_z \end{pmatrix} = \varepsilon_0 \begin{pmatrix} \chi^{(2)}_{11} & \chi^{(2)}_{12} & \chi^{(2)}_{13} & 0 & \chi^{(2)}_{15} & 0 \\ 0 & 0 & 0 & \chi^{(2)}_{24} & 0 & \chi^{(2)}_{26} \\ \chi^{(2)}_{31} & \chi^{(2)}_{32} & \chi^{(2)}_{33} & 0 & \chi^{(2)}_{35} & 0 \end{pmatrix} \begin{pmatrix} E^2cos^2(\theta) \\ E^2sin^2(\theta) \\ 0 \\ 0 \\ 0 \\ 2Ecos(\theta)\sin(\theta) \end{pmatrix} \qquad (S4)$$

Where the first subscript 1 = *x*, 2 = *y* and 3 = *z*; the second subscript 1 = *xx*, 2 = *yy*, 3 = *zz*, 4 = *yz*, 5 = *xz* and 6 = *xy*. In our calculations, the x direction is defined as the spontaneous polarization direction, i.e., *c*-axis, and the y direction is aligned to the *b*-axis. The x and y directions lie in the plane, while the z direction is perpendicular to the *xy* plane. One can see that the SHG intensity of WO_2Br_2 is dominated by the components $\chi^{(2)}_{11}$, $\chi^{(2)}_{12}$, and $\chi^{(2)}_{26}$ under the back-reflection configuration, and the value of each component has been calculated through DFT calculations, which is shown on the figure and table below:

Supplementary Table 3 DFT calculated values of independent elements in the WO_2Br_2 second-order optical susceptibility tensor

Component	2ω Frequnecy (eV)	real part (pm/V)	imaginary part (i pm/V)
$\chi_{11}^{(2)}$	2.4	54.9	-369.5
$\chi_{12}^{(2)}$	2.4	-49.1	-99.9
$\chi_{26}^{(2)}$	2.4	-36.3	4.3

Moreover, P in x and y directions is given by:

$$P_x = \chi_{11}^{(2)} cos^2(\theta) + \chi_{12}^{(2)} sin^2(\theta) \quad (S5)$$

$$P_y = 2\chi_{26}^{(2)} cos(\theta) sin(\theta) \quad (S6)$$

$$P_z = 0 \quad (S7)$$

The SHG intensity under different configurations can be expressed by the following formula:

$$I_{total} \propto \left(\begin{pmatrix} P_x \\ P_y \\ P_z \end{pmatrix} \cdot (1 \quad 1 \quad 0) \right)^2 \quad (S8)$$

$$I_{para} \propto \left(\begin{pmatrix} P_x \\ P_y \\ P_z \end{pmatrix} \cdot (\cos\theta \quad \sin\theta \quad 0) \right)^2 \quad (S9)$$

$$I_{perp} \propto \left(\begin{pmatrix} P_x \\ P_y \\ P_z \end{pmatrix} \cdot (-\sin\theta \quad \cos\theta \quad 0) \right)^2 \quad (S10)$$

Substituting the numerical values into the formula for calculation, the intensity of SHG under different configurations of DFT computation and the comparison with the experimental results can be obtained, as shown in the **Supplementary Fig. 24**. After normalizing these results and comparing them with the normalized results obtained from actual experiments (with the phases of theoretical and experimental results aligned before comparison), it can be seen that the two are almost completely consistent. Further analysis of the parallel and perpendicular components reveals that the parallel component is also nearly identical to the theoretical calculations, while there is some discrepancy in the perpendicular component. This may be related to the fact that the electric field in the z-direction and the P component are not entirely zero in the actual experiment, as well as depolarization caused by optical components. Since the signal

in the perpendicular direction is weaker, it may be more susceptible to these factors. Despite some discrepancies, the pattern of intensity variation is consistent, with the SHG polar intensity exhibiting a "four-lobed" shape. The analysis results considering point group symmetry indicate that our theoretical calculations align well with the experiments, and the polarization measurement data are largely consistent with the expected optical anisotropy.

By incorporating calculated elements of the second-order nonlinear susceptibility tensor into these equations, we obtain theoretical polarization-dependent SHG polar plots that align with experimental results. In analyzer-free (total) and parallel configurations, SHG intensity maxima occur along the *c*-axis direction, while minima align with the *b*-axis, which establish an experimental foundation for precise identification of crystallographic axes.

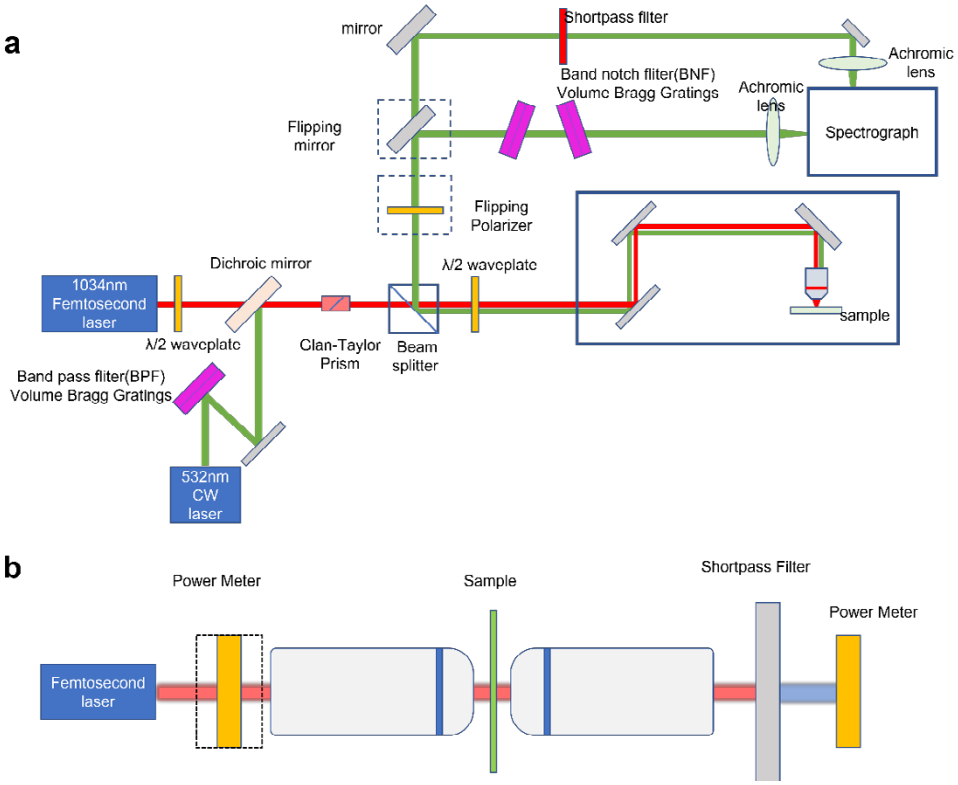

Supplementary Fig. 23 Optical paths configurations in different experiments. (a) Optical configuration for in-situ SHG and Raman spectra; (b) Optical configuration for SHG conversion efficiency measurement.

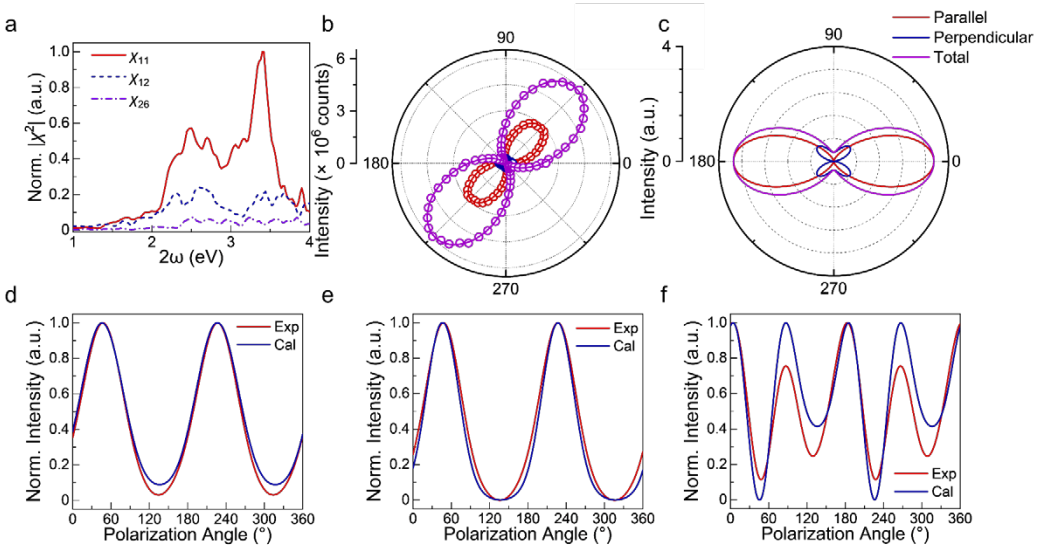

Supplementary Fig. 24 Comparison between DFT-calculated and experimental SHG responses of WO_2Br_2. (a) DFT-calculated wavelength dependence of the independent SHG tensor components contributing to the signal in a back-reflection geometry. (b) Experimentally measured polarization-resolved SHG patterns in the parallel, perpendicular, and total detection configurations. (c) Theoretical SHG patterns for the same three configurations, constructed from the DFT-calculated independent tensor components. (d–f) Direct comparison between experimental and theoretical results for the total (d), parallel (e), and perpendicular (f) configurations, all normalized.

2. SHG intensity of WO_2Br_2

The relationship between experimentally measured SHG intensity and second-order susceptibility coefficient is governed by[20–23]

$$I(2\omega) = \frac{2\omega^2}{c^3\varepsilon_0 n^2(\omega)n(2\omega)} \cdot \left(\chi^{(2)}\right) I^2(\omega)T^2 \frac{sin^2(\Delta k \cdot T/2)}{(\Delta k \cdot T/2)^2} \qquad (S11)$$

For ultrathin 2D materials where phase-matching constraints are automatically satisfied, the expression simplifies to:

$$I(2\omega) = \frac{2\omega^2}{c^3\varepsilon_0 n^2(\omega)n(2\omega)} \cdot \left(\chi^{(2)}\right)^2 I^2(\omega)T^2 = k \cdot \frac{\left(\chi^{(2)}\right)^2}{n^2(\omega)n(2\omega)} \cdot I^2(\omega) \qquad (S12)$$

This relation shows that, by measuring the power-dependent SHG intensities of a sample with unknown second-order nonlinear susceptibility and a reference sample with known susceptibility, and then comparing the slopes of the SHG-intensity versus pump-power-squared plots, one can extract the SHG second-order susceptibility of the unknown sample. To determine the SHG second-order susceptibility of WO_2Br_2, $NbOI_2$ with a known $\chi^{(2)}$was chosen as the reference material[23], and power-dependent SHG measurements were performed for both materials, as shown in **Supplementary Fig. 25**. Consequently, the slope ratio of pump-power-squared vs SHG-intensity plots between two materials becomes:

$$\frac{k_{NbOI_2}}{k_{WO_2Br_2}} = \frac{\left(\chi^{(2)}_{NbOI_2}\right)^2}{\left(\chi^{(2)}_{WO_2Br_2}\right)^2} \frac{n^2_{WO_2Br_2}(\omega)n_{WO_2Br_2}(2\omega)}{n^2_{NbOI_2}(\omega)n_{NbOI_2}(2\omega)} \qquad (S13)$$

Here, $n(\omega)$ and $n(2\omega)$ denote the refractive indices at the fundamental and SHG frequencies, respectively. The refractive indices of $NbOI_2$ are taken from the literature, whereas those of WO_2Br_2 are obtained from first-principles calculations.

By incorporating refractive indices[24]

$$n_{WO_2Br_2}(517\ nm) = 2.9, n_{WO_2Br_2}(1034\ nm) = 2.6$$

$$n_{NbOI_2}(517\ nm) = 2.1, n_{NbOI_2}(1034\ nm) = 2.6$$

$$\chi^{(2)}_{NbOI_2} = 190\ pm/V$$

One can generate that

$$\chi^{(2)}_{WO_2Br_2} = 120\ pm/V$$

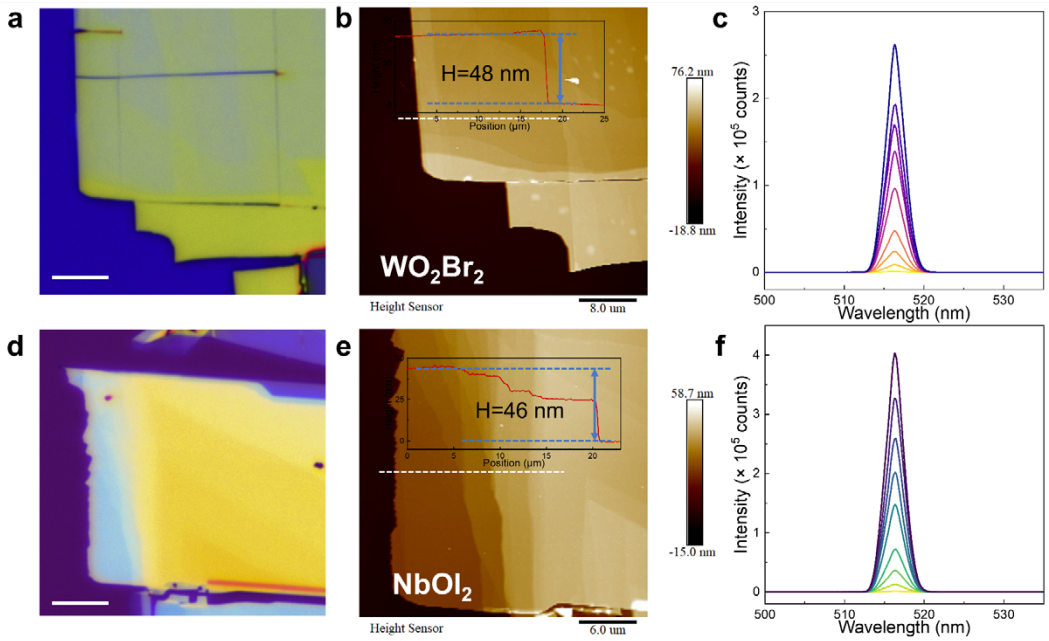

Supplementary Fig. 25 WO_2Br_2 and $NbOI_2$ samples for $\chi^{(2)}$ susceptibility calibration with corresponding SHG spectra under 1034 nm excitation. (a), (b) and (c) Optical image, AFM image and SHG spectra for WO_2Br_2; (d), (e) and (f) for $NbOI_2$. Scale bar in a and d: 10 μm.

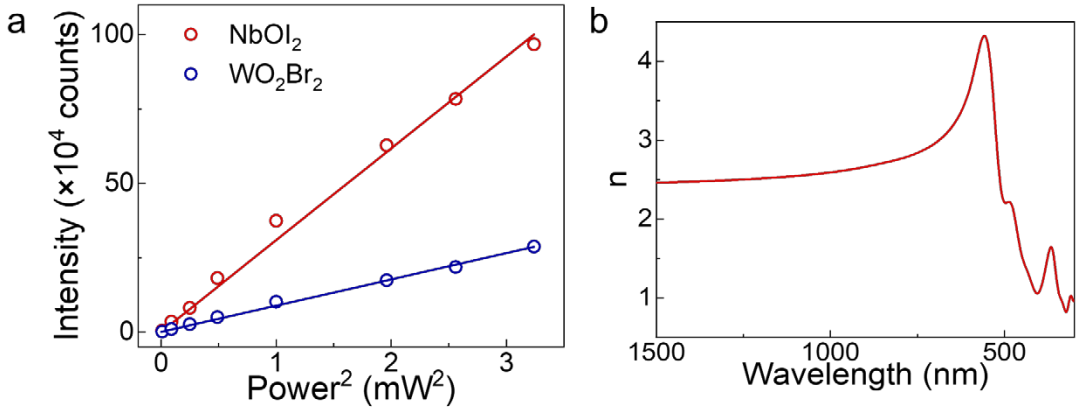

Supplementary Fig. 26 (a) Power dependence of SHG intensity in WO_2Br_2 and $NbOI_2$, revealing a slope ratio of 3.49:1 (b) DFT-calculated refractive index of WO_2Br_2 along the polar axis.

3. Intensity gradient of SHG response in WO_2Br_2

For pristine WO_2Br_2, the SHG intensity gradient mainly arises from morphological factors such as thickness variations and bubbles introduced during the transfer process. We measured polarization-resolved SHG for WO_2Br_2 over thicknesses from about 10 nm to about 500 nm (comparable to the emission wavelength), as shown in **Supplementary Fig. 27** and **Supplementary Fig. 28**. The polarization plots maintain the same orientation across different thicknesses; fit results show that the polar axis angles differ by no more than 5° (96°-100°), indicating that any birefringence-induced rotation of the collected SHG axis is negligible within the thickness range of the sample which used for hydrostatic pressure experiments (70-130 nm), in particular, 45° or 90° rotations which were found during hydrostatic pressure applying cannot be accounted for by the intrinsic birefringence of the samples. In addition, SHG imaging shows that samples of the same thickness without morphological defects exhibit spatially uniform SHG intensity, which further rules out the influence of twinning and buried domains.

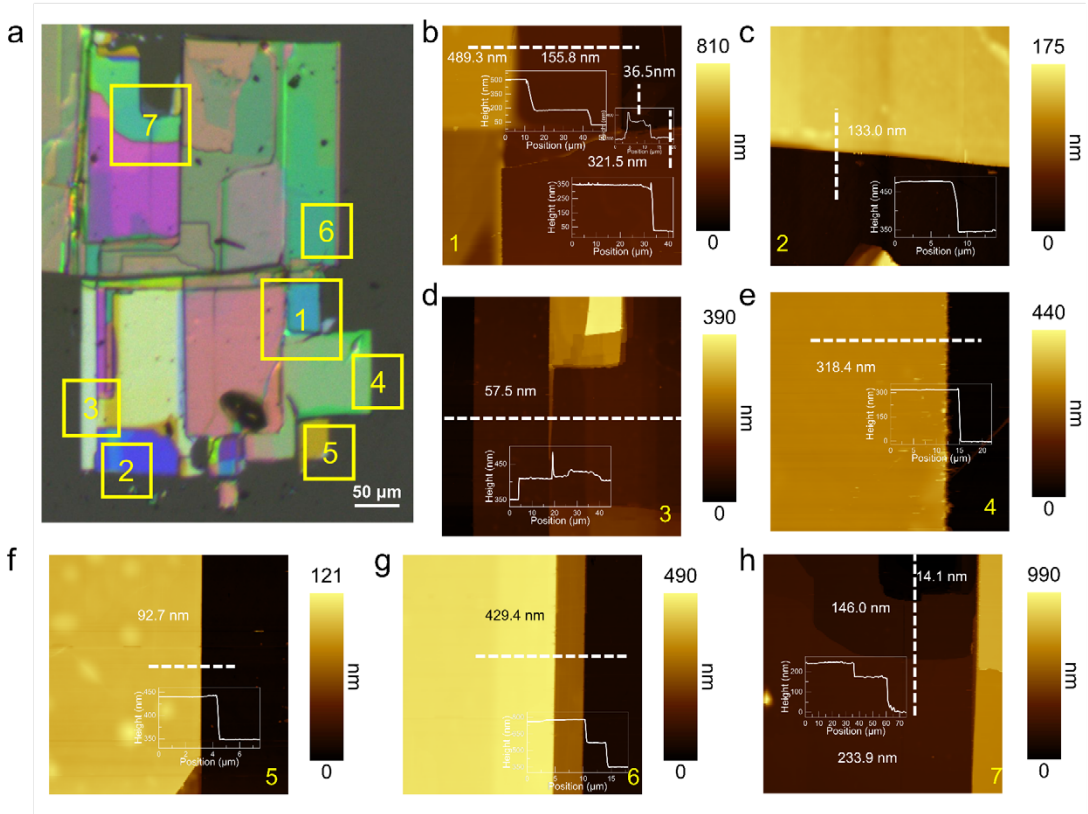

Supplementary Fig. 27 Optical morphology and AFM characterization of the WO_2Br_2 flakes used for SHG measurements. (a) Optical micrograph of the sample. (b–h) AFM height images of the selected regions, from which the flake thickness is determined; the corresponding areas are indicated in the lower-left corner of each AFM panel.

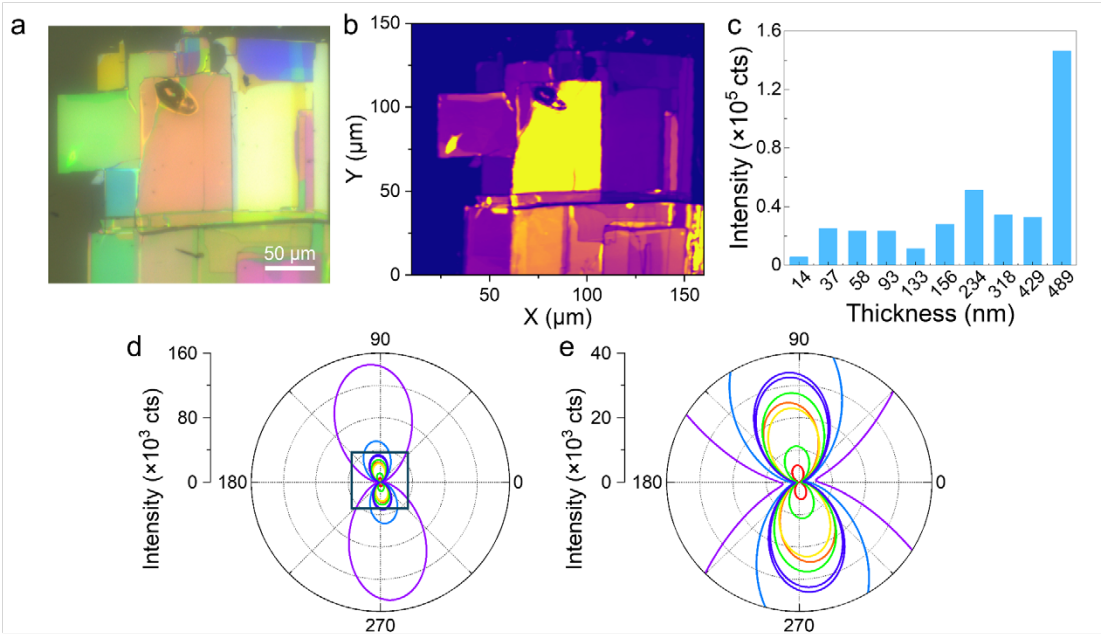

Supplementary Fig. 28 SHG spectral imaging of WO_2Br_2 and comparison of SHG intensity and polarization patterns for different flake thicknesses. (a) Optical micrograph of the sample. (b) SHG spectral image; the polarization of the excitation beam is aligned with the polar axis to maximize the SHG intensity. (c) SHG intensity of flakes with different thicknesses when the laser polarization is parallel to the polar axis. (d, e) Polarization-resolved SHG patterns corresponding to different positions marked in (c), with (e) corresponding to the region highlighted by the blue box in (d).

4. SHG response of WO_2Br_2 under applied strain and electric field

Using substrate bending to apply uniaxial tensile strain, we find that the SHG intensity of WO_2Br_2 decreases with increasing strain, whereas the orientation of the SHG polar axis does not rotate within our accessible strain range (~1.6%), indicating that canting the polarization axis would require a larger driving force. For bent beams the surface strain can be approximated as $\varepsilon \approx t/(2R)$[25], where t is the substrate thickness and R is the bending radius, which provides an upper bound for the strain delivered by our flexible-substrate geometry. The absence of an axis rotation here therefore implies that the in-plane polarization direction in WO_2Br_2 remains lattice-locked under our uniaxial tensile loading conditions.

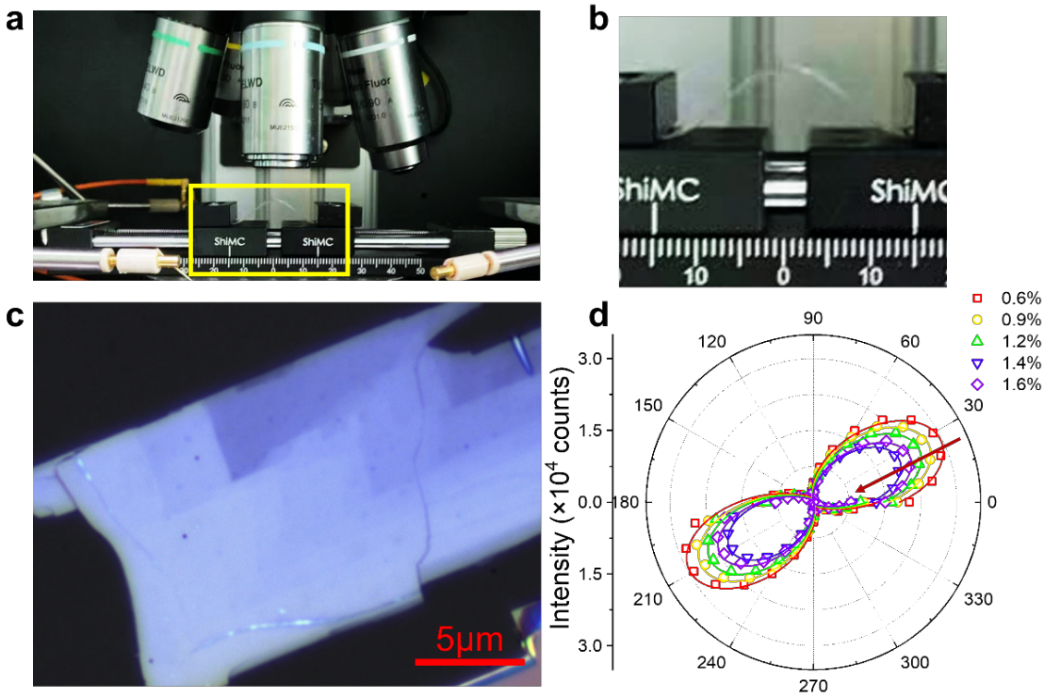

Supplementary Fig. 29 Polarization-dependent SHG of WO_2Br_2 under uniaxial tensile strain. (a) strain application stage integrated with in situ optical measurement setup; (b) Uniaxial tensile strain generation via curved substrate bending; (c) Optical image of sample mount for strain-modulated SHG measurements; (d) Polarization-resolved SHG polar plots under progressively increased strain levels. Details of the strain-calculation methodology can be found in our previous work

After determining the crystal orientation of the WO_2Br_2 flake by polarization-resolved SHG, we transferred it onto a two-terminal device with Au electrodes, aligning the applied electric field along the non-polar (*b*) axis. Both polarized optical microscopy and polarization-resolved SHG confirm that, in the absence of an external field, the WO_2Br_2 flake does not contain domains with other in-plane orientations; the slight spatial variation in SHG intensity mainly arises from bubbles introduced during the

transfer process and from SHG enhancement at the Au interface. Upon applying an electric field, we recorded polarization-resolved SHG patterns at different positions within the channel, as shown in **Supplementary Fig. 30**. The results indicate that an electric field applied along the *b*-axis has only a limited influence on the SHG intensity. Moreover, such a field does not induce a reorientation of the WO_2Br_2 polar axis from the *c*-axis toward the *b*-axis: the SHG intensity projected along the *b*- direction remains at a comparable level for different field strengths. This demonstrates that no polarization-axis switching from *c*- to *b*- occurs in WO_2Br_2 under an electric field applied along the *b*- axis.

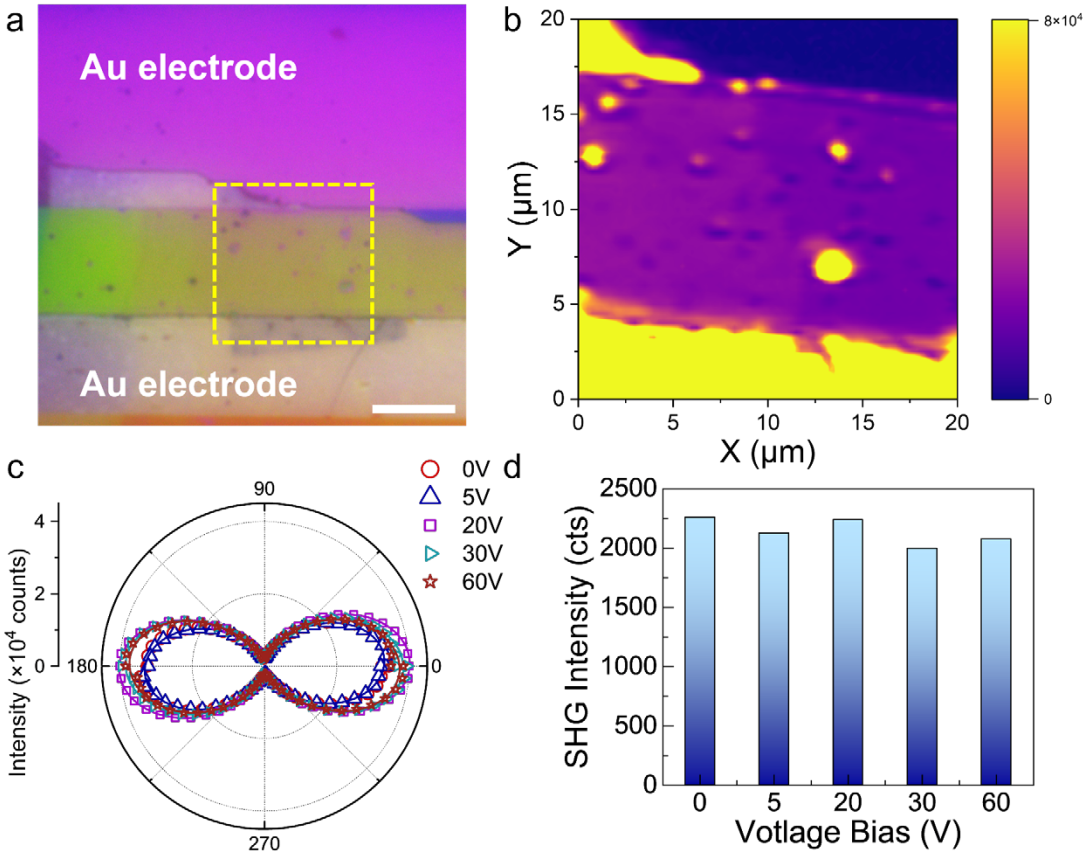

Supplementary Fig. 30 Polarization-dependent SHG response of WO_2Br_2 under an applied in-plane electric field. (a) Polarized optical micrograph of the device; the yellow dashed box marks the region where SHG mapping is performed. (b) SHG image of the selected region in (a) at zero bias. Enhanced SHG responses are observed in bubble regions and on the Au substrate. (c) Polarization-resolved SHG polar plots under different bias voltages. (d) SHG intensity along the non-polar-axis direction. Scale bar in (a): 20 μm

Supplementary V. Hydrostatic Pressure of WO_2Br_2

1. Polarized optical micrographs and SHG spectra of WO_2Br_2 under hydrostatic pressure

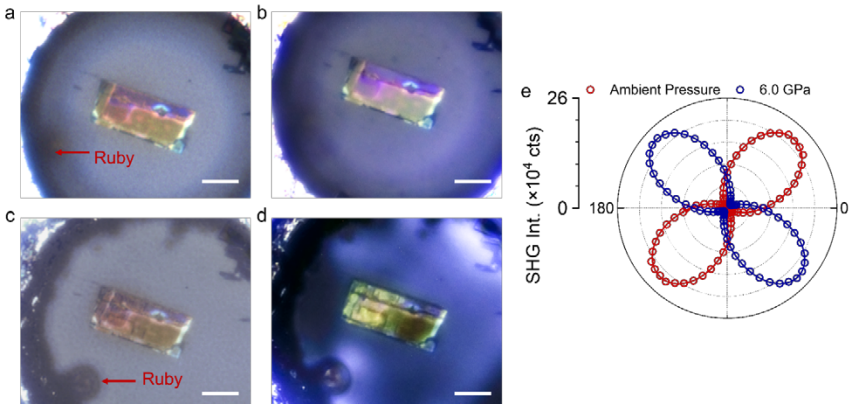

Supplementary Fig. 31 (a, b) Unpolarized (a) and polarized (b) optical images at ambient pressure. (c, d) Unpolarized (c) and polarized (d) optical images at 6.0 GPa. Scale bar: 20 μm (e) Polarized SHG of the same region generated at ambient pressure and 6.0 GPa.

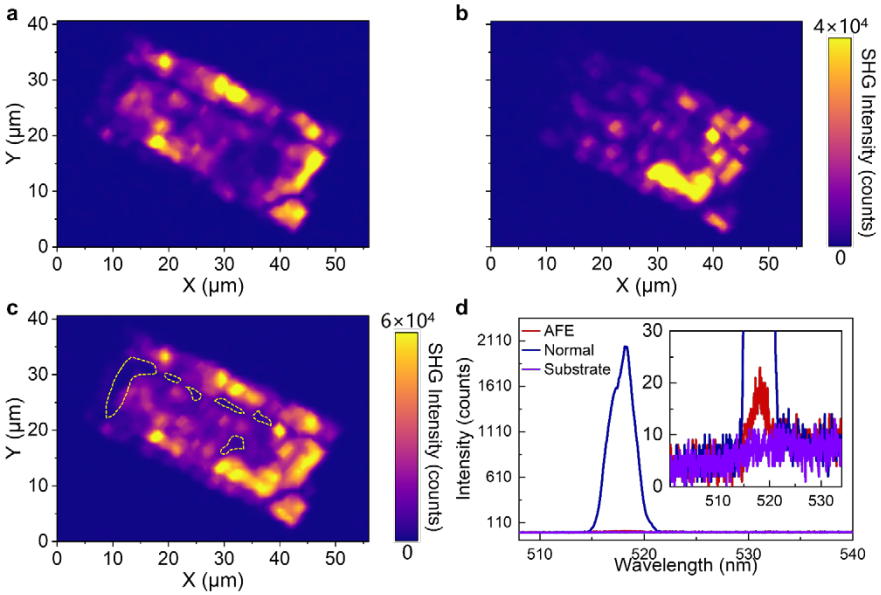

Supplementary Fig. 32 SHG intensity mappings at 6.0 GPa along ***E*** // *c* (a) and ***E*** // *b* (b), and their summed image (c). Overlaying SHG mappings from both the polar and nonpolar directions eliminate the possibility that the observed intensity reduction arises from polarization reorientation. Regions that remain low in intensity after summation are outlined with yellow dashed lines. (d) displays SHG spectra collected from representative positions corresponding to the substrate, antiferroelectric region, and normal region in the summed image. The antiferroelectric region exhibits a significantly reduced SHG signal, approximately 1% of that in the normal region, which is attributed to the spatial inhomogeneity of the phase transition and the large laser spot size, as discussed in the main text.

2. Possible 90° polarization-switching pathways in WO_2Br_2 (noncollinear and collinear structures)

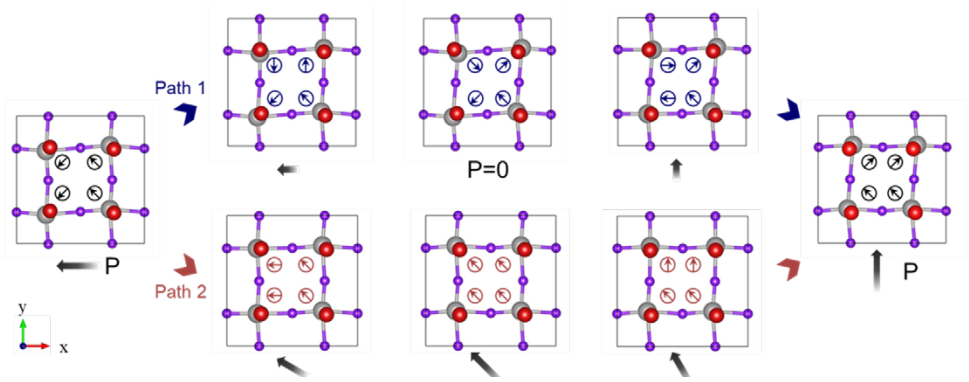

Supplementary Fig. 33 The crystal structures corresponding to each marked point in the energy diagram in **Fig. 4b.**

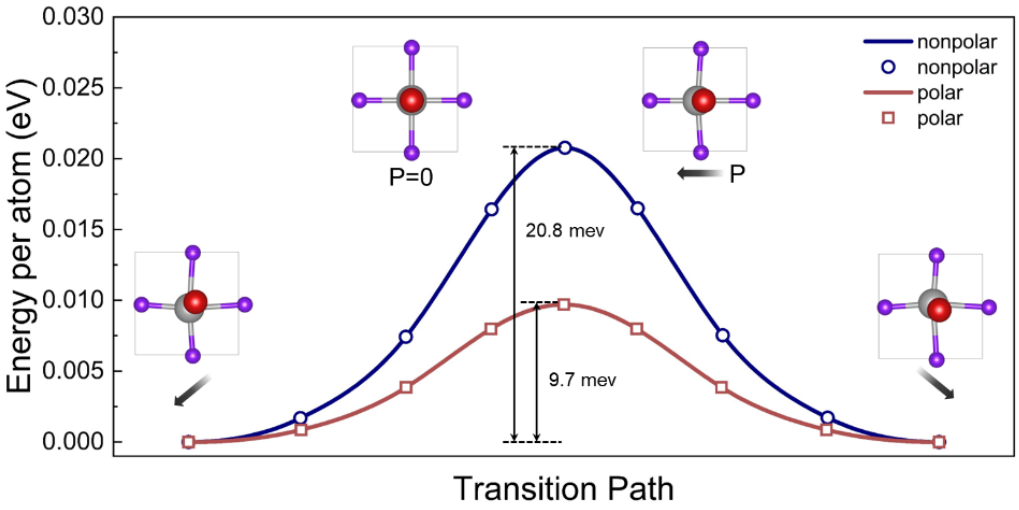

Supplementary Fig. 34 Energy and atomic structure transition path of the collinear dipole model. Energy paths show non-degenerate single-barrier features. The energy barriers are 2 to 4 times larger compared with those of the experimental noncolinear structure (5.7 and 5.8 meV).

3. Structural evolution of WO_2Br_2 under hydrostatic pressure

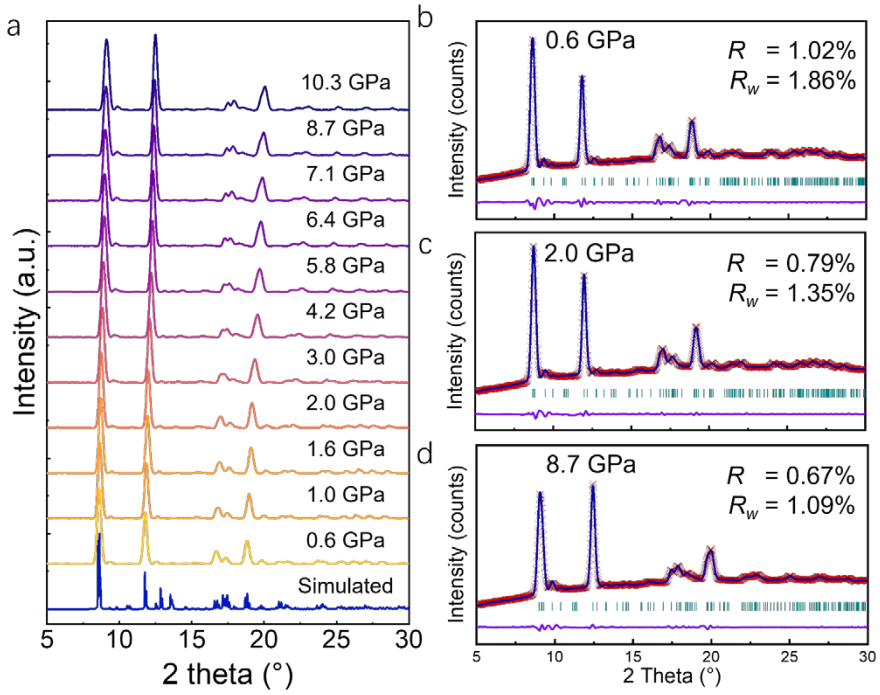

Supplementary Fig. 35 Powder XRD patterns of WO_2Br_2 under high pressure. (a) Powder XRD patterns of WO_2Br_2 at different pressures. (b–d) *Le Bail* refinements of the diffraction profiles at several representative pressures.

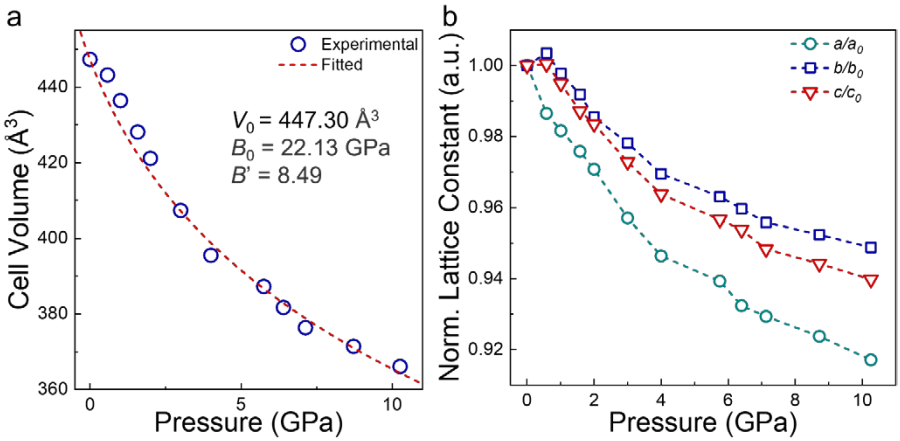

Supplementary Fig. 36 Pressure-dependent lattice parameters of *Le Bail* refinement. (a) Pressure evolution of unit cell volume; (b) Pressure evolution of three lattice axes with the a-axis along the van der Waals stacking direction.

The pressure-induced reduction of unit cell volume follows a smooth monotonic trend, with the third-order Birch-Murnaghan equation of state (BM-EOS) providing a bulk modulus of 22.13 GPa and a pressure derivative of 8.49. Anisotropic lattice compression is particularly evident in the van der Waals stacking direction, significantly

exceeding in-plane lattice shrinkage which serves as a hallmark of layered materials characterized by weak interlayer interactions.

Supplementary Table 4 The crystallographic data generated from the single-crystal XRD of WO_2Br_2 under 5.0 GPa

Crystal Data	
Chemical formula	Br2O2W
Mr	375.67
Crystal system, space group	Orthorhombic, *Pcc2*
Temperature (K)	296
a, b, c (Å)	7.4988(7), 27.983(18), 7.3364(10)
α, β, γ (°)	90, 90, 90
V(Å^3)	1539.5(10)
Z	18
Radiation type	Mo *Kα*
μ(mm^{-1})	50.59
No. of measured, independent and observed [$I > 2\sigma(I)$] reflections	2411, 460, 276
R_{int}	0.090
$(\sin\theta/\lambda)_{max}$ (Å^{-1})	0.582
$R[F^2 > 2\sigma(F^2)]$, $wR(F^2)$, S	0.183, 0.492, 1.93
No. of reflections	460
No. of parameters	46
No. of restraints	2
$\Delta\rho_{max}$, $\Delta\rho_{min}$ (e/Å^3)	5.01, −3.51

High-pressure (HP) single-crystal XRD demonstrates a *Cc*→*Pcc2* transition in WO_2Br_2 near 5.0 GPa, while the corresponding powder patterns show no abrupt change in peak positions or profiles, consistent with a subtle structural adjustment. The metric evolution is small: the axis that was *b* at ambient becomes *a* in the high-pressure setting. In addition, four octahedra lie along *b*-axis in HP phase rather than two in ambient pressure phase, and the lattice constants shrink from 3.86450 Å to 3.74940 Å (HP phase *a*-direction) and from 7.68010 Å to 7.33640 Å (*c*-axis), with the interlayer spacing

decreasing from 7.493 Å to 6.995 Å (HP phase *b*-direction) as expected under compression. The high-pressure phase remains non-centrosymmetric and polar, in full agreement with the clear SHG response observed in the same pressure range.

The apparent discrepancy between powder and single-crystal diffraction stems from their different sensitivities to structural changes. One-dimensional powder patterns—particularly in a diamond-anvil-cell environment, where non-hydrostatic stress, grain refinement, and preferred orientation can broaden and overlap peaks—are intrinsically less sensitive to subtle symmetry changes. By contrast, single-crystal X-ray diffraction exploits the full three-dimensional reciprocal space and intensity constraints to resolve the space group and associated distortions. Therefore, the powder XRD patterns show no obvious peak anomalies, whereas single-crystal XRD clearly identifies the change in space group. The continuous evolution of the one-dimensional diffraction profiles, together with the similarity between the high-pressure and ambient-pressure Raman spectra (**Supplementary Fig. 41**, **Supplementary Fig. 42**), further indicates that the pressure-induced transition is a gradual and moderate structural evolution rather than a drastic atomic rearrangement.

The structural schematics of HP phase together with the refined cell parameters are given in **Supplementary Table 4** and **Supplementary Fig. 37**. On this basis, we performed a layer-by-layer analysis of the high-pressure *Pcc2* structure, as shown in **Supplementary Fig. 38**. Along the layer-normal direction, the atoms can be grouped into a series of parallel layers. The high-pressure structure contains four crystallographically independent layers, whose distortion patterns are not identical. A common feature is that all layers retain the relative displacement between W and Br atoms along the *c*-direction, indicating that the spontaneous polarization along *c*-axis is preserved. In layers 1 and 3, the alternating W displacements along *a*-axis (which corresponds to the antipolar *b*-axis of the ambient-pressure *Cc* structure in the new setting) vanish; accordingly, these layers can be regarded as losing the noncollinear polarization character. In layers 2 and 4, tilting of the Br atoms induces distortions of the octahedra, yet the staggered W displacements along the *a*-axis remain, suggesting that the noncollinear configuration is retained in these layers. Therefore, the high-pressure phase is not a trivial case of either fully preserving or completely losing the noncollinear polarization; instead, it exhibits a gradual structural evolution in which noncollinear features persist in part of the structure.

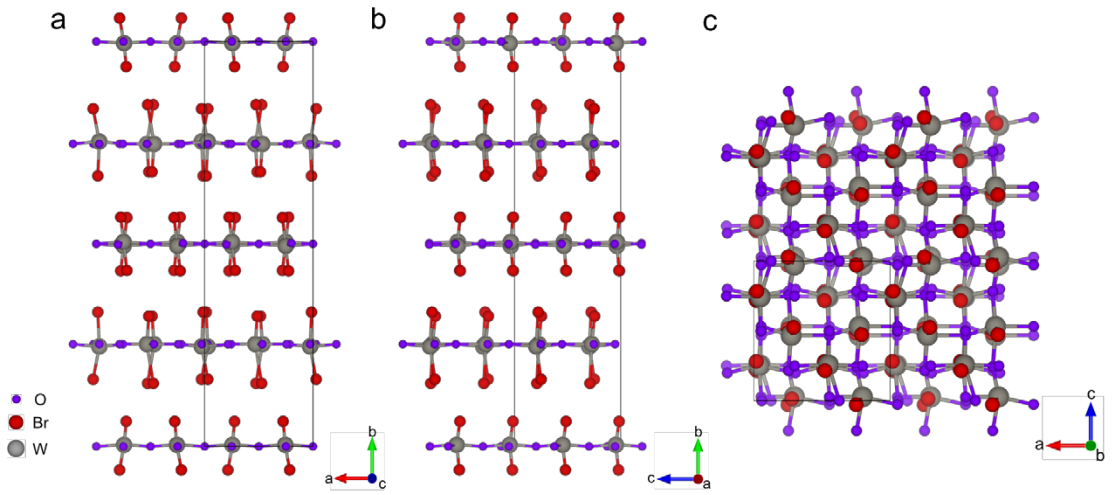

Supplementary Fig. 37 Schematic crystal structure of WO_2Br_2 at 5.0 GPa. (a–c) Structural projections viewed along the a, c, and b axes, respectively.

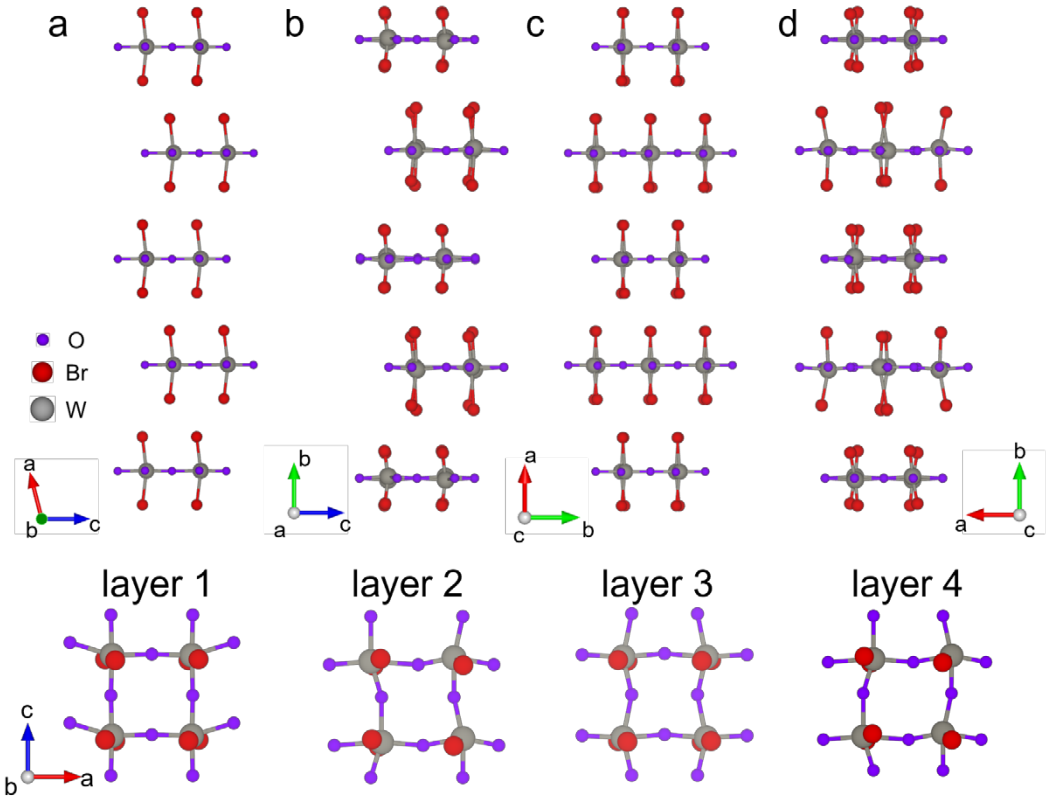

Supplementary Fig. 38 Schematic comparison between the ambient-pressure WO_2Br_2 structure and the high-pressure phase, with projections along the *b*-axis illustrating the four independent atomic layers in the high-pressure phase. (a, c) Ambient pressure phase; (b, d) High Pressure phase; bottom panel: schematic of independent atomic layers in the high-pressure phase along the *b*-axis.

4. Raman spectra of WO_2Br_2 under hydrostatic pressure

WO_2Br_2 crystallizes in the *Cc* space group with 10 atoms per unit cell, supporting 30 phonon modes (27 optical modes), all of which are Raman-active and represented as 13A' + 14A", where A' and A" denote irreducible representations. **Supplementary Table 5** summarizes the calculated phonon modes with corresponding Raman vibrational mode assignments based on their computed frequencies. The vibrational mode assignments were systematically analyzed through polarized Raman spectroscopy combined with group-theoretical symmetry analysis, with detailed discussions presented below.

Supplementary Table 5 Raman-active modes and vibrational frequencies of WO_2Br_2 obtained from DFT calculations; experimentally observed modes are highlighted in green.

Phonon Mode	Calculated energy (cm^{-1})	Irreducible representation	Experimental energy (cm^{-1})
1	0	A'	
2	0	A"	
3	0	A'	
4	51.12	A'	
5	60.19	A"	
6	69.20	A"	
7	83.64	A'	
8	85.40	A"	
9	86.51	A"	
10	86.90	A'	
11	89.81	A'	93.8
12	90.52	A"	
13	115.77	A'	123.5
14	193.24	A"	
15	232.76	A'	234.9
16	240.20	A"	
17	247.01	A"	
18	257.02	A'	

19	278.12	A'	
20	292.64	A"	
21	327.69	A'	272.9
22	335.55	A"	
23	339.66	A'	338.6
24	353.35	A"	
25	371.91	A"	
26	402.28	A'	
27	691.34	A'	
28	742.47	A"	739.9
29	777.00	A'	815.6
30	970.36	A"	

The *Cc* space group belongs to the m point group (*Cs* symmetry). For this point group, the Raman tensors corresponding to Raman-active modes under light absorption conditions adopt the following irreducible representation:

$$\boldsymbol{R}(\boldsymbol{A'}) = \begin{bmatrix} |a|e^{i\varphi_a} & 0 & 0 \\ 0 & |b|e^{i\varphi_b} & |c|e^{i\varphi_c} \\ 0 & |c|e^{i\varphi_c} & |d|e^{i\varphi_d} \end{bmatrix} \quad (S14)$$

$$\boldsymbol{R}(\boldsymbol{A''}) = \begin{bmatrix} 0 & |e|e^{i\varphi_e} & |f|e^{i\varphi_f} \\ |e|e^{i\varphi_e} & 0 & 0 \\ |f|e^{i\varphi_f} & 0 & 0 \end{bmatrix} \quad (S15)$$

The experimentally measured polarized Raman intensities can be quantitatively determined by symmetry selection rules and scattering geometry configurations. The fundamental relationship between Raman intensity $\boldsymbol{I}$ and polarization states of incident $\boldsymbol{e_i}$ and scattered $\boldsymbol{e_s}$ light is expressed as:

$$\boldsymbol{I} = |\boldsymbol{e_s} \cdot \boldsymbol{R} \cdot \boldsymbol{e_i}|^2 \quad (S16)$$

where $\boldsymbol{R}$ represents the Raman tensor of the specific phonon mode. We define the experimental geometry with both laser incidence and Raman signal detection along the z axis (perpendicular to the *bc*-plane). In this coordinate system, the crystallographic *b* axis is aligned with the laboratory x axis, and the *c* axis with the y axis. Under parallel polarization configuration, the polarization vectors satisfy $\boldsymbol{e_s} = \boldsymbol{e_i} = (\boldsymbol{cos\theta}, \boldsymbol{sin\theta}, \boldsymbol{0})$, where $\boldsymbol{\theta}$ denotes the in-plane polarization angle relative to the *b* axis. For perpendicular configuration, the relationship becomes $\boldsymbol{e_i} = (\boldsymbol{cos\theta}, \boldsymbol{sin\theta}, \boldsymbol{0})$ and $\boldsymbol{e_s} = (\boldsymbol{-sin\theta}, \boldsymbol{cos\theta}, \boldsymbol{0})$.

The Raman intensities of A' and A" modes under both polarization configurations can be derived as:

$$I_{A'}^{\parallel} \propto a^2 \cos^4(\theta) + b^2 \sin^4(\theta) + 2|a||b| \cos^2(\theta) \sin^2(\theta) \cos(\varphi_{a-b}) \quad (S17)$$

$$I_{A'}^{\perp} \propto \frac{\sin^2(2\theta)}{4}(a^2 + b^2 - 2ab \cos(\varphi_{a-b})) \quad (S18)$$

$$I_{A''}^{\parallel} \propto e^2 \sin(2\theta)^2 \quad (S19)$$

$$I_{A''}^{\perp} \propto e^2 \cos(2\theta)^2 \quad (S20)$$

For the A" mode, the polarized Raman intensity is expected to show a π/2 period. In contrast to the Raman peak at 739.9 cm^{-1}, all other ambient-pressure Raman peaks exhibit π-periodicity under parallel polarization configurations, enabling their identification as A' modes. Through systematic cross-checking with theoretically calculated peak positions, we conclusively assign the 739.9 cm^{-1} Raman feature to the A" mode.

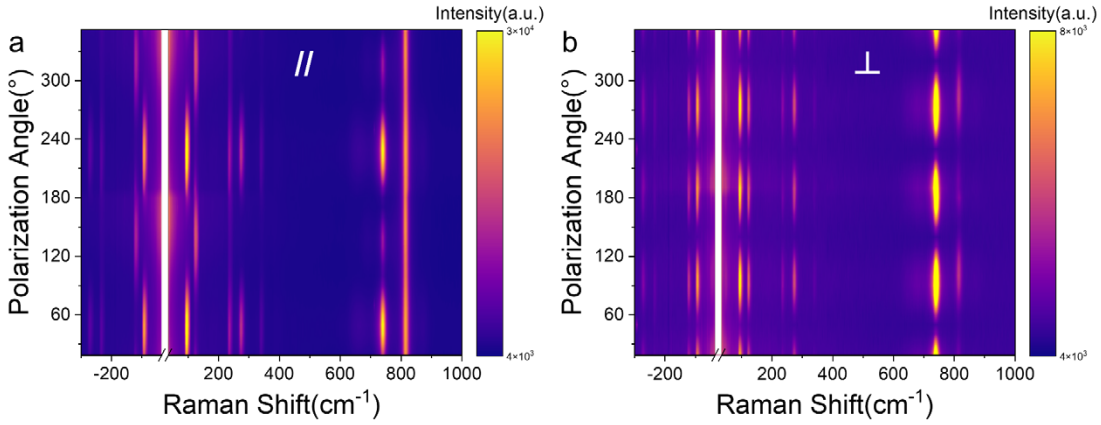

Supplementary Fig. 39 Polarization-dependent Raman spectroscopy of WO_2Br_2 (a) Parallel configuration; (b) Perpendicular configuration.

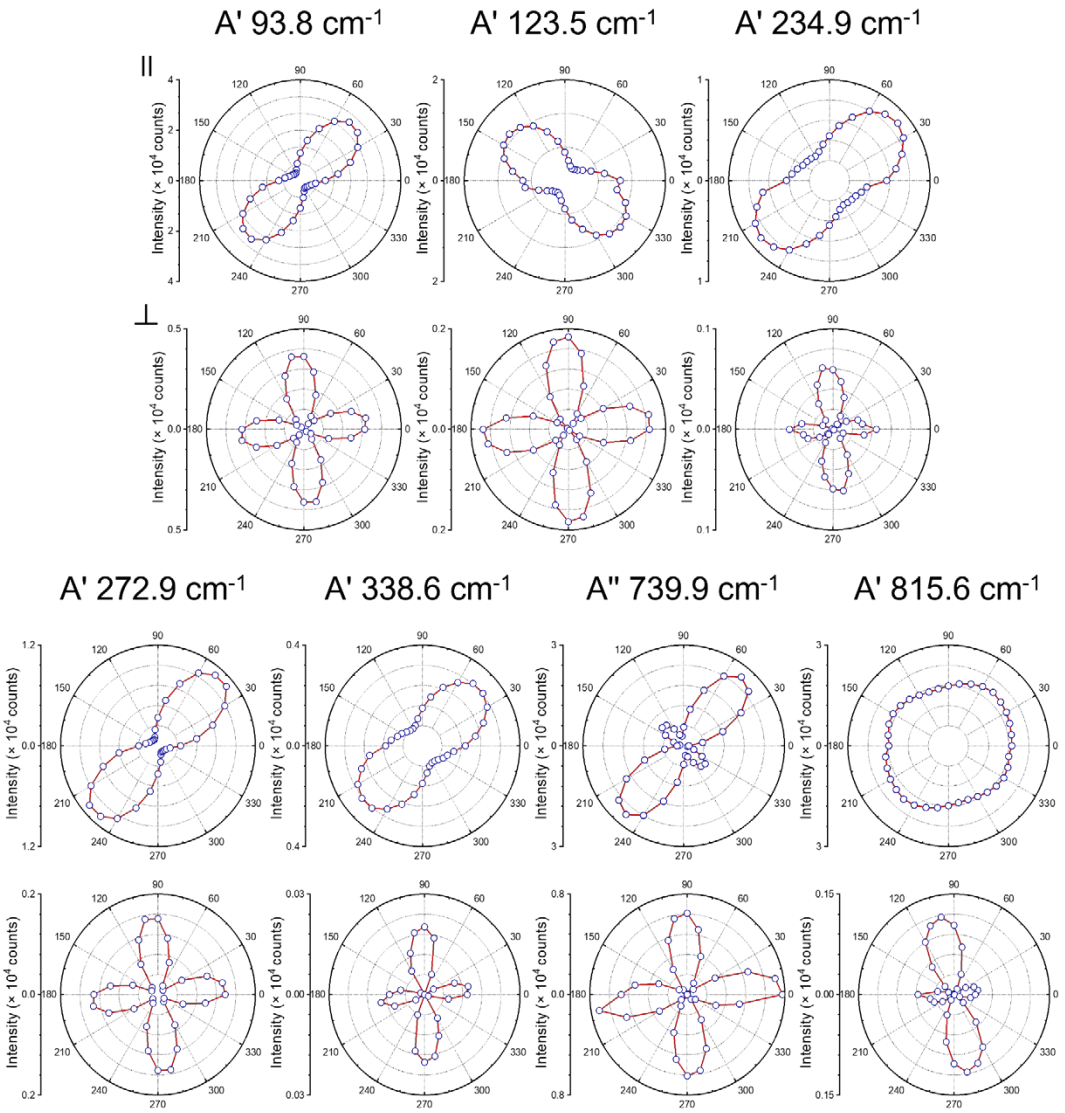

Supplementary Fig. 40 Polarization-resolved Raman polar plots for parallel and perpendicular configurations

We selected the AP transition pathway as a representative and investigated the structural evolution of WO_2Br_2 under pressure using *in-situ* Raman spectroscopy. presents a contour plot of the pressure-dependent Raman spectra. As shown in **Supplementary Fig. 41**, pressure-induced structural evolution exhibits two key characteristics: (1) the emergence of additional vibrational modes at 77.0 cm^{-1} (1.1 GPa), 109.8 cm^{-1} (2.4 GPa), 181.6 cm^{-1} (2.4 GPa), 254.9 cm^{-1} (4.0 GPa), and 733.1 cm^{-1} (2.4 GPa). Among these, the modes at 77.0, 109.8, and 733.1 cm^{-1} vanish above 5.0 GPa, indicating the formation and subsequent disappearance of a metastable phase upon pressure. (2) the continuous detectability of all ambient-pressure Raman features throughout the compression process implies that the original vibrational framework is largely preserved. Notably, at 6.0 GPa, the Raman spectrum closely resembles that at ambient pressure, suggesting that the structure stabilizes into a

noncollinear dipolar configuration under high pressure, confirming that reversible metastable states dominate the compression-induced transition pathway.

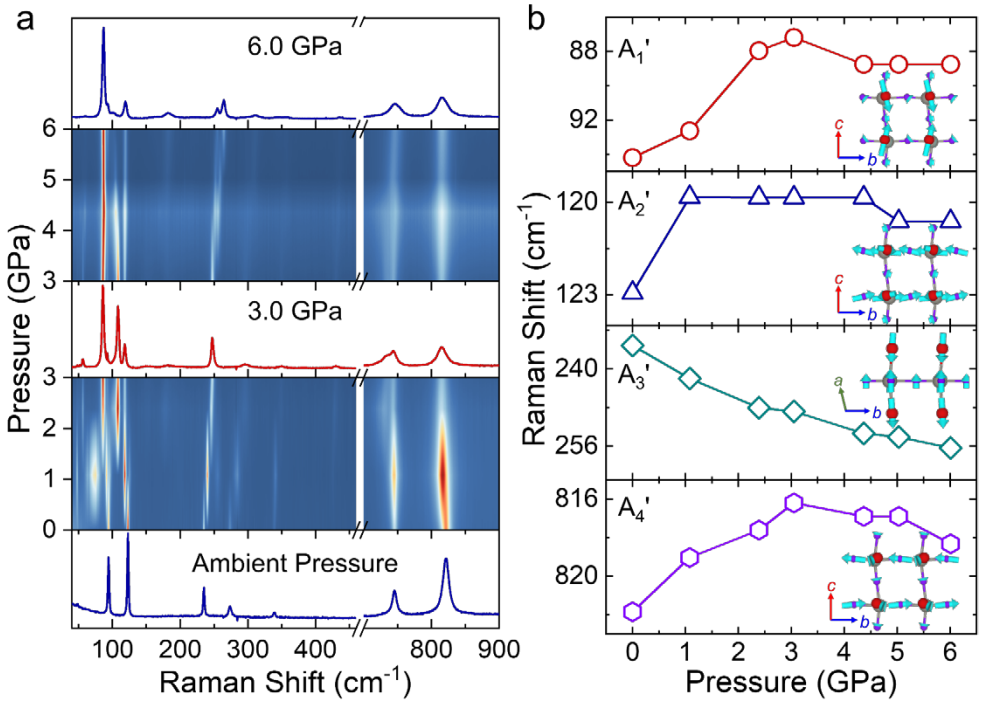

Supplementary Fig. 41 Evolution of the Raman modes of WO_2Br_2 under high pressure. (a) False-colour map showing the evolution of the Raman spectrum of WO_2Br_2 as a function of pressure; Raman spectra at three representative pressures are overlaid. (b) Pressure dependence of four representative Raman modes (A'$_1$, 93.8 cm^{-1}; A'$_2$, 123.5 cm^{-1}; A'$_3$, 234.9 cm^{-1}; A'$_4$, 815.6 cm^{-1}).

The variation of phonon frequencies provides additional insights into the structural evolution of WO_2Br_2 under high pressure. Bond force constants vary under compression, giving rise to pressure-dependent shifts in vibrational frequencies. In our experiment, pressure-dependent frequency shifts of four representative vibrational modes—designated A'$_1$ to A'$_4$—located at 93.8 123.5, 234.9, and 815.6 cm^{-1} (**Supplementary Fig. 41**), were clearly identified. Specifically, the A'$_1$, A'$_2$, and A'$_4$ modes are primarily governed by in-plane bond vibrations, whereas the A'$_3$ mode originates from out-of-plane vibrational components. For the out-of-plane A'$_3$ mode, a continuous blueshift is observed with increasing pressure, indicating sustained compression along the out-of-plane direction[26–28]. In contrast, the in-plane modes A'$_1$, A'$_2$, and A'$_4$ exhibit anomalous frequency evolution, in which the vibrational frequencies initially undergo a redshift below 3.0 GPa and then experience a blueshift above this pressure. This behavior suggests in-plane bond softening or lattice expansion below 3.0 GPa[29,30]. Such anomalous response correlates well with the emergence of a metastable phase observed via pressure-activated Raman modes, as well as the formation of an AP intermediate phase identified in SHG measurements. Upon further

compression, the A'_1, A'_2, and A'_4 modes shift toward higher frequencies, indicating a recover to conventional pressure-induced bond stiffening. This transition coincides with the disappearance of the metastable phase and the recovery of SHG intensity. The sustained blue shift of the out-of-plane mode confirms that the formation of the intermediate phase is governed predominantly by in-plane atomic rearrangements, consistent with theoretical predictions.

According to our calculations, in the ambient-pressure Raman spectrum of WO_2Br_2 the peak at 93.8 cm^{-1} corresponds to the ferroelectric vibrational mode, whereas the peak at 123.5 cm^{-1} corresponds to the antiferroelectric vibrational mode. These two modes exist as distinct features at ambient pressure, and polarization-resolved Raman measurements in the parallel configuration reveal an approximately 90° phase difference between them. Under high pressure, the orientation of the crystal has changed 90°, and both vibrational modes remain observable (**Supplementary Fig. 42**), and polarization-resolved Raman spectroscopy indicates that the ~90° phase difference is also preserved. Therefore, we infer that the ferroelectric and antiferroelectric vibrational modes are retained under high pressure and continue to exhibit an approximately 90° orientational difference. This serves as indirect evidence supporting the persistence of a noncollinear structural state at high pressure.

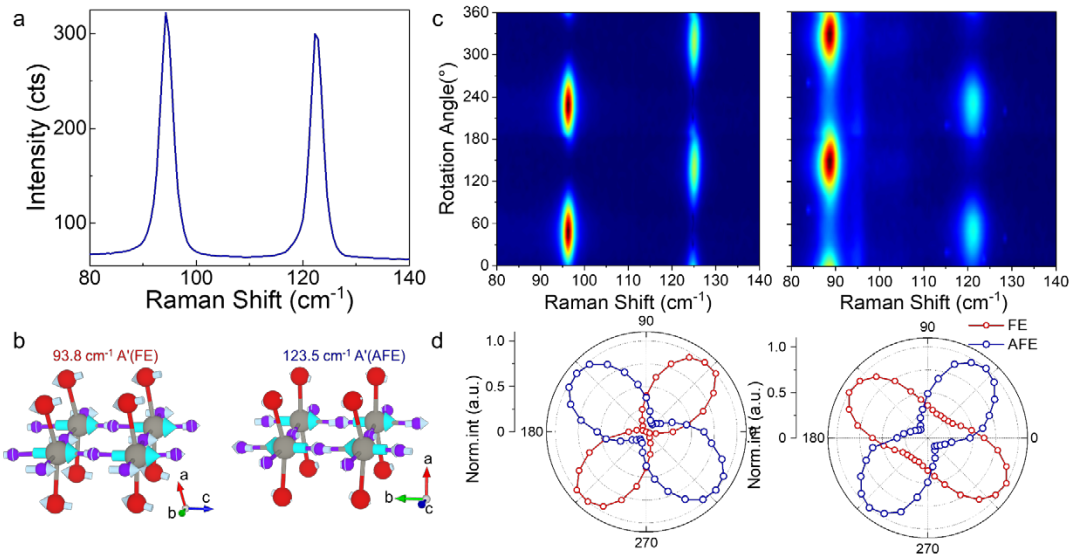

Supplementary Fig. 42 (a, b) Two representative Raman vibrational modes of WO_2Br_2 at ambient pressure and the corresponding schematic atomic displacement patterns. (c) False-colour maps of polarization-resolved Raman spectra of the ferroelectric and antiferroelectric modes at ambient pressure (left) and 6.0 GPa (right). (d) Polar plots of the polarization-resolved Raman intensities of the ferroelectric and antiferroelectric modes at ambient pressure (left) and at 6.0 GPa (right).

5. Crystal structure, domain structure, and domain-wall stability of WO_2Br_2 after the pressurization–decompression cycle

According to the above analysis, the noncollinear electric dipole in WO_2Br_2 leads to the 90° polarization rotation process under pressure, which enables an effective strategy of domain or domain wall engineering. However, the micrometer-scale anvil faces of DAC fundamentally constrain sample dimensions. To circumvent this, we implement ultrahard tungsten carbide anvils for millimeter-scale sample loading-unloading cycles[31], achieving bulk-scale domain engineering. **Supplementary Fig. 43b** presents the mechanically exfoliated samples of pressure-treated crystals, exhibiting bright/dark contrast under polarized light microscope, which presents two types of domains with a ~90° orientation difference from polarization-resolved SHG measurements (**Supplementary Fig. 43bc**). Both domains (designated domains 1 and 2) display Raman peaks identical to those of pristine prepared WO_2Br_2 (**Supplementary Fig. 44**) confirming preservation of the crystal structure, consistent with the electron diffraction results (**Supplementary Fig. 45**).

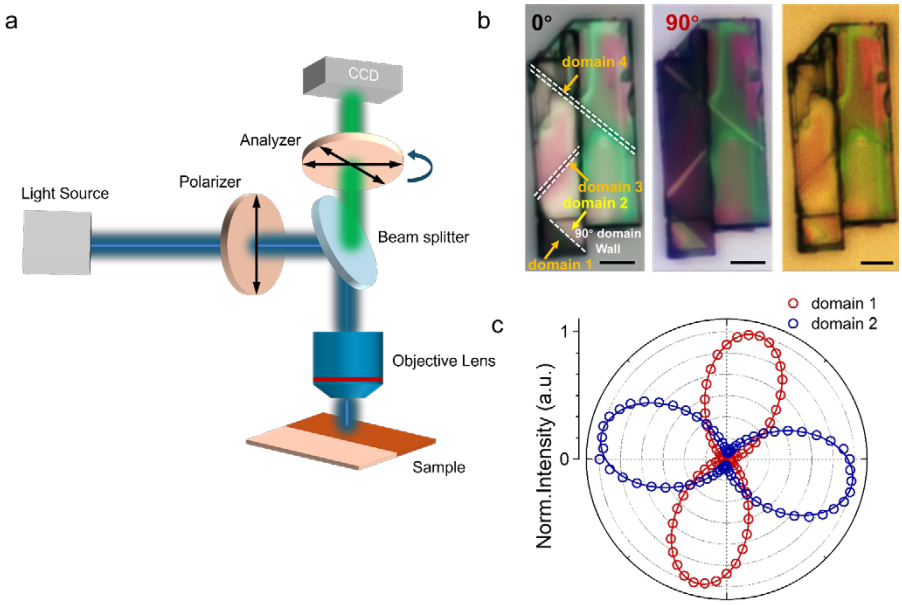

Supplementary Fig. 43 Polarized optical microscopy and polarization-resolved SHG patterns of WO_2Br_2 after hydrostatic pressure treatment. (a) Schematic of the polarized optical microscopy configuration. (b) Optical micrographs of WO_2Br_2 after hydrostatic pressure treatment, from left to right: polarized image with the analyzer at 0°, polarized image with the analyzer at 90°, and unpolarized image. (c) Polarization-resolved SHG patterns from the regions labeled domain 1 and domain 2 in (b). Scale bar in (b): 10 μm.

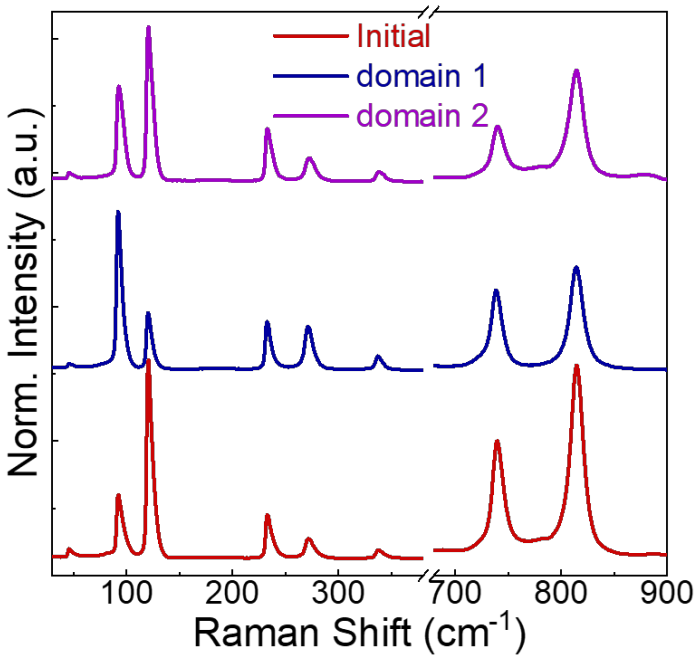

Supplementary Fig. 44 Raman spectra of initial WO_2Br_2, domain 1 and domain 2 in **Supplementary Fig. 43**

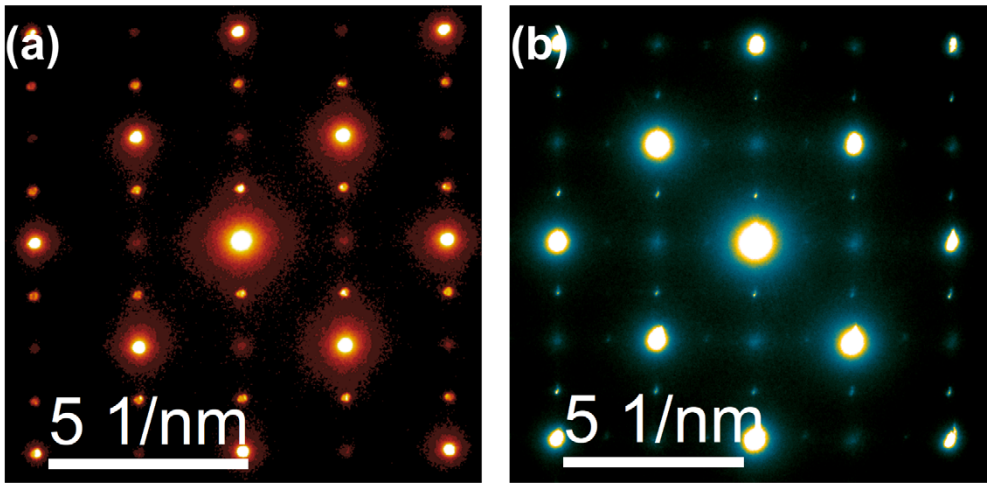

Supplementary Fig. 45 Selected-area electron diffraction (SAED) patterns of pristine WO_2Br_2 and WO_2Br_2 after high-pressure treatment (b), both taken along the [201] zone axis. The additional diffraction spots observed in SAED arise from multiple scattering.

Remarkably, the domain walls exhibited exceptional energy stability: neither thermal annealing (up to 240°C) nor uniaxial tensile strain ($\varepsilon \approx 2\%$) induced changes in domain proportions, indicating the existence of a high critical energy barrier for orientation reversal, as theoretically predicted and experimentally revealed. In samples where 90° domains are difficult to form initially, pressure therefore creates 90° domains that remain after release. In this sense, pressure serves as a handle for domain control.

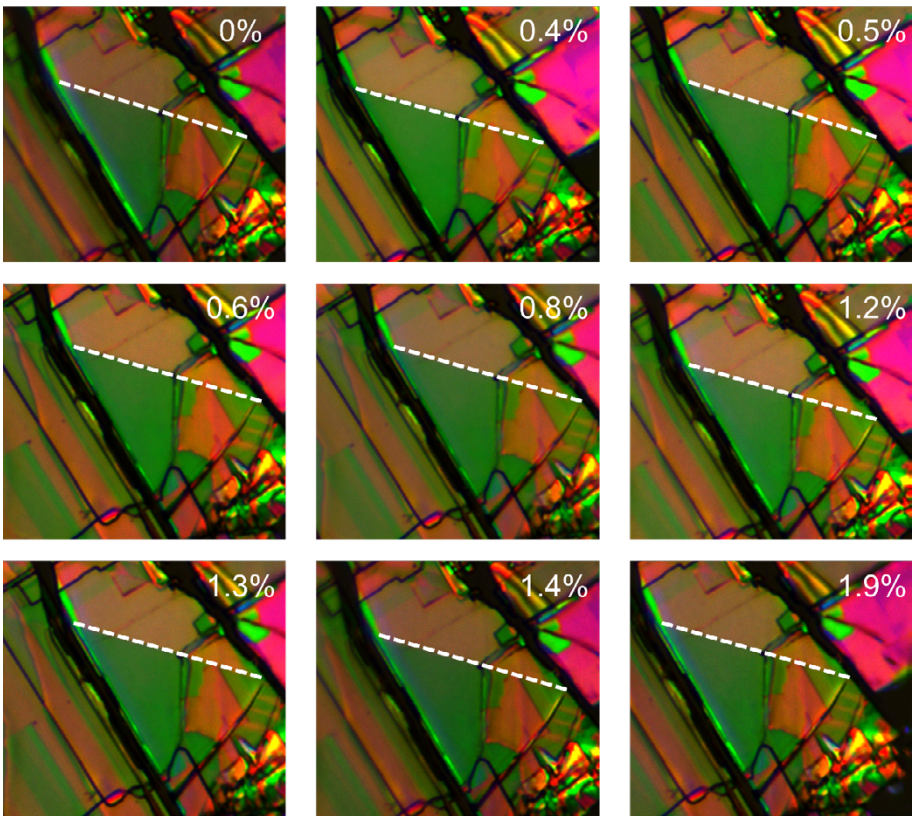

Supplementary Fig. 46 Domain evolution under uniaxial strain in a high-pressure-treated sample with 90° domains. Domain walls exhibit negligible movement across applied strain levels.

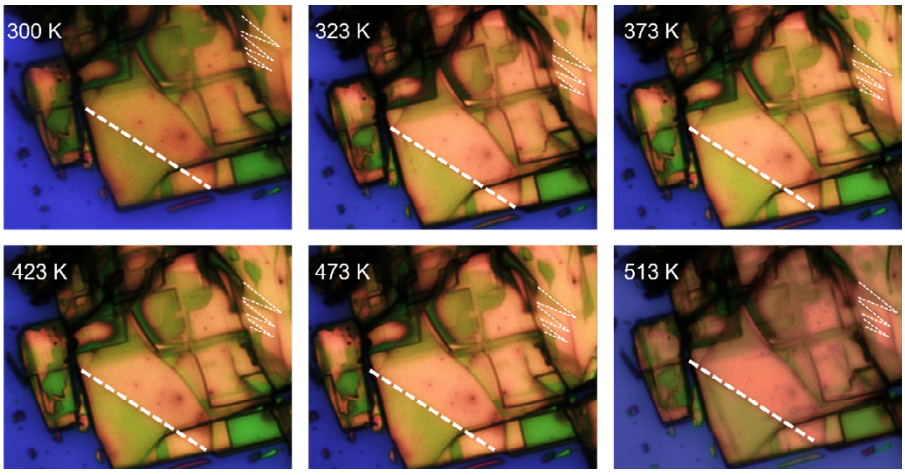

Supplementary Fig. 47 Domain evolution at varied temperatures in high-pressure-treated samples with 90° domains. Negligible domain wall movement under heating with persistent domains throughout thermal cycling, demonstrating stability of domain structure.

Supplementary VI. UED of WO_2Br_2

In the ultrafast electron diffraction experiment, we use 400 nm femtosecond laser pusle to excitate (above-gap excitation) the thin film WO_2Br_2 sample. With normal incidence of the electron pusel to the sample surface, several coherent phonon modes are superimposed on the intensity change of Bragg reflections. Besides the 2.70 THz and 3.70 THz phonon modes, another coherent phonon mode with the frequency of 1.20 THz is observed, as shown in **Supplementary Fig. 48a-b**. This low frequency phonon mode also displays in the Raman spectrum in **Supplementary Fig. 48c** while is absent in our DFT simulation. So this phonon mode may derive from the interlayer shear mode or local dipole vortices, which will be identified further in the future work. To decompose these phonon modes, we tilt the sample by ~ 5 degree off the normal incidence. In this case, we get clearly 2.70 THz and 3.70 THz phonon mode in separate Bragg reflections, as shown in **Supplementary Fig. 48d-f.** The intensity oscillations in **Figs. 5c-5f** in the main text derive from the intensity decay in **Supplementary Fig. 48e-f** substracting an monoexponential fit.

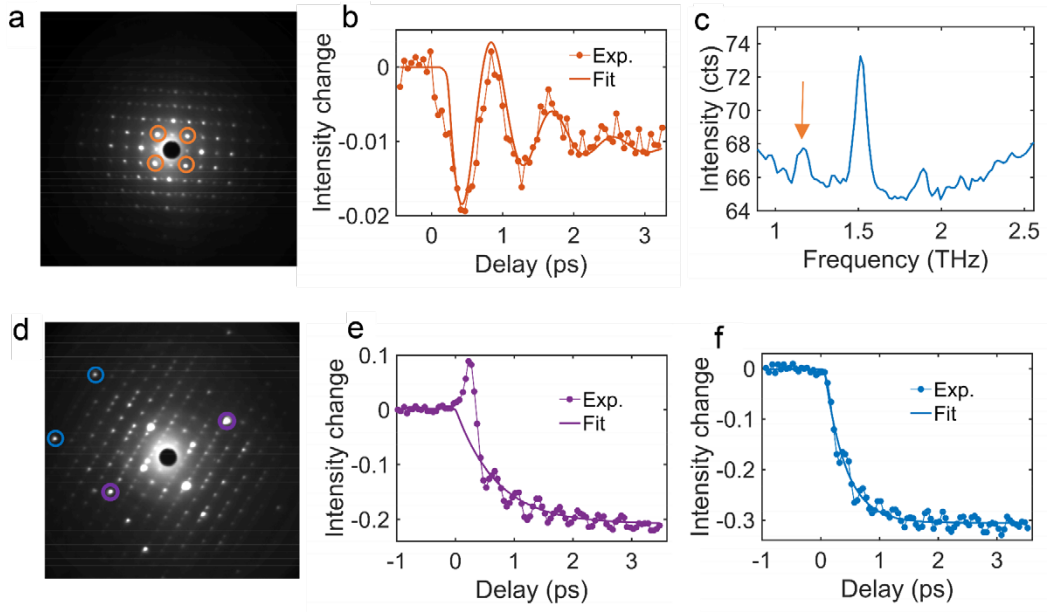

Supplementary Fig. 48 (a) Diffraction pattern with normal incidence of electron pulse to the sample surface. The {112} crystal plane diffraction peaks are indicated by yellow circles. (b) Intensity changes of the {112} diffraction peaks labeled with yellow circles in (a). The solid line is the fit with an oscillation frequency of 1.20 THz. (c) Raman spectrum of the 1.20 THz phonon mode indicated by the yellow arrow. (d) Diffraction pattern with an oblique angle of ~5 degree off the normal incidence. (e) Intensity change of diffraction peaks labeled with the purple circles in (d). The solid line is the fit with a monoexponential function. (f) Intensity changes of diffraction peaks labeled with the blue circles in (d). The solid line is the fit with a monoexponential function.

Reference

1. Campanini, M. *et al.* Atomic-resolution differential phase contrast STEM on ferroelectric materials: A mean-field approach. *Phys. Rev. B* **101**, 184116 (2020).
2. Müller, K. *et al.* Atomic electric fields revealed by a quantum mechanical approach to electron picodiffraction. *Nat. Commun.* **5**, 5653 (2014).
3. Lin, L.-F., Zhang, Y., Moreo, A., Dagotto, E. & Dong, S. Frustrated Dipole Order Induces Noncollinear Proper Ferrielectricity in Two Dimensions. *Phys. Rev. Lett.* **123**, 067601 (2019).
4. Aroyo, M. I. *et al.* Bilbao crystallographic server: I. Databases and crystallographic computing programs. *Z. Für Krist. - Cryst. Mater.* **221**, 15–27 (2006).
5. Kroumova, E. *et al.* PSEUDO : A program for a pseudosymmetry search. *J. Appl. Crystallogr.* **34**, 783–784 (2001).
6. Orobengoa, D., Capillas, C., Aroyo, M. I. & Perez-Mato, J. M. AMPLIMODES: Symmetry-mode analysis on the bilbao crystallographic server. *J. Appl. Crystallogr.* **42**, 820–833 (2009).
7. Scott, C. A. M. & Bristowe, N. C. Universal polar instability in highly orthorhombic perovskites. *J. Am. Chem. Soc.* **146**, 29735–29741 (2024).
8. Zhang, Y., Wang, J. & Ghosez, P. Unraveling the suppression of oxygen octahedra rotations in A3B2O7 ruddlesden-popper compounds: Engineering multiferroicity and beyond. *Phys. Rev. Lett.* **125**, 157601 (2020).
9. Balke, N. *et al.* Deterministic control of ferroelastic switching in multiferroic materials. *Nat. Nanotechnol.* **4**, 868–875 (2009).
10. Baek, S. H. *et al.* Ferroelastic switching for nanoscale non-volatile magnetoelectric devices. *Nat. Mater.* **9**, 309–314 (2010).
11. Cui, C. *et al.* Intercorrelated in-plane and out-of-plane ferroelectricity in ultrathin two-dimensional layered semiconductor In2se3. *Nano Lett.* **18**, 1253–1258 (2018).

12. Xiao, J. *et al.* Intrinsic two-dimensional ferroelectricity with dipole locking. *Phys. Rev. Lett.* **120**, 227601 (2018).
13. Xue, F. *et al.* Room-temperature ferroelectricity in hexagonally layered α-In_2Se_3 nanoflakes down to the monolayer limit. *Adv. Funct. Mater.* **28**, 1803738 (2018).
14. Han, W. *et al.* Phase-controllable large-area two-dimensional In2Se3 and ferroelectric heterophase junction. *Nat. Nanotechnol.* **18**, 55–63 (2023).
15. Wu, Y. *et al.* Data-driven discovery of high performance layered van der waals piezoelectric NbOI2. *Nat. Commun.* **13**, 1884 (2022).
16. Liu, C. *et al.* Ferroelectricity in niobium oxide dihalides NbOX2 (X = cl, I): A macroscopic- to microscopic-scale study. *ACS Nano* acsnano.2c09267 (2023).
17. Yan, Q. *et al.* Ambient Degradation Anisotropy and Mechanism of van der Waals Ferroelectric NbOI2. *ACS Appl. Mater. Interfaces* **16**, 9051–9059 (2024).
18. Wang, Y. *et al.* Ultrafast dynamics of ferroelectric polarization of NbOI2 captured with femtosecond electron diffraction. *Nat. Commun.* **16**, 8132 (2025).
19. Hossain, M. S. *et al.* Conducting Domain Walls in van der Waals Ferroelectric NbOI2. *Nano Lett.* (2025).
20. Ma, C. *et al.* Strong chiroptical nonlinearity in coherently stacked boron nitride nanotubes. *Nat. Nanotechnol.* 1–7 (2024).
21. Guo, Q. *et al.* Ultrathin quantum light source with van der waals NbOCl2 crystal. *Nature* **613**, 53–59 (2023).
22. Xu, X. *et al.* Towards compact phase-matched and waveguided nonlinear optics in atomically layered semiconductors. *Nat. Photonics* (2022).
23. Abdelwahab, I. *et al.* Giant second-harmonic generation in ferroelectric NbOI2. *Nat. Photonics* **16**, 644–650 (2022).

24. Fang, Y., Wang, F., Wang, R., Zhai, T. & Huang, F. 2D NbOI2 : A chiral semiconductor with highly in-plane anisotropic electrical and optical properties. *Adv. Mater.* **33**, 2101505 (2021).
25. Liang, J. *et al.* Monitoring local strain vector in atomic-layered MoS2 by second-harmonic generation. *Nano Lett.* **17**, 7539–7543 (2017).
26. Feng, X. *et al.* Giant tunability of charge transport in 2D inorganic molecular crystals by pressure engineering. *Angew. Chem.* **135**, e202217238 (2023).
27. Tang, L. *et al.* Giant piezoresistivity in a van der waals material induced by intralayer atomic motions. *Nat. Commun.* **14**, 1519 (2023).
28. Yao, X. Anomalous polarization enhancement in a van der waals ferroelectric material under pressure. *Nat. Commun.* **14**, 4301 (2023).
29. Xia, J. *et al.* Pressure-induced phase transition in weyl semimetallic WTe2. *Small* **13**, 1701887 (2017).
30. Fu, T. *et al.* Manipulating Peierls Distortion in van der Waals NbOX2 Maximizes Second-Harmonic Generation. *J. Am. Chem. Soc.* **145**, 16828–16834 (2023).
31. Chen, D. *et al.* General approach for synthesizing hexagonal diamond by heating post-graphite phases. *Nat. Mater.* 1–6 (2025).